Leveraging virtues of circular and oval shapes in multi-orifice synthetic jet flow and heat transfer characteristics

M. Tech. Thesis

By

Janupala Chakradhar Reddy

(Roll No.: 2202103034)

DEPARTMENT OF MECHANICAL ENGINEERING

INDIAN INSTITUTE OF TECHNOLOGY INDORE

MAY 2024

Leveraging virtues of circular and oval shapes in multi-orifice synthetic jet flow and heat transfer characteristics

A THESIS

Submitted in partial fulfillment of the requirements for the award of the degree
of
Master of Technology

in

Thermal Energy Systems

by

Janupala Chakradhar Reddy

(Roll No.: 2202103034)

DEPARTMENT OF MECHANICAL ENGINEERING

INDIAN INSTITUTE OF TECHNOLOGY INDORE

MAY 2024

INDIAN INSTITUTE OF TECHNOLOGY INDORE

CANDIDATE'S DECLARATION

I hereby certify that the work which is being presented in the thesis entitled **Leveraging virtues of circular and oval shapes in multi-orifice synthetic jet flow and heat transfer characteristics** in the partial fulfilment of the requirements for the award of the degree of **MASTER OF TECHNOLOGY** in **THERMAL ENERGY SYSTEMS** and submitted in the **DEPARTMENT OF MECHANICAL Indian Institute of Technology Indore** is an authentic record of my own work carried out during the time period from July 2022 to May 2024 under the supervision of Dr. Satyanarayan Patel, Associate Professor, and Dr. Harekrishna Yadav, Assistant Professor, Department of Mechanical Engineering, IIT Indore.

The matter presented in this thesis has not been submitted by me for the award of any other degree of this or any other institute.

Signature of the student with date

JANUPALA CHAKRADHAR REDDY

This is to certify that the above statement made by the candidate is correct to the best of my/our knowledge.

Signature of the Supervisor of M.Tech. thesis #1 (with date)
(Dr. Satyanarayan Patel)

Signature of the Supervisor of M.Tech. thesis #2 (with date)
(Dr. Harekrishna Yadav)

JANUPALA CHAKRADHAR REDDY (Roll No.: 2202103034) has successfully given his/her M.Tech. Oral Examination held on **May 30 2024**.

Signature(s) of Supervisor(s) of M.Tech. thesis
(Dr. Satyanarayan Patel) Date: 04/06/2024

Signature(s) of Supervisor(s) of M.Tech. thesis
(Dr. Harekrishna Yadav) Date: 04/06/2024

Convener, DPGC
Date: 07/06/2024

ACKNOWLEDGEMENT

I would like to express my deepest gratitude to my supervisor, **Dr. Satyanarayan Patel** and co-supervisor **Dr. Harekrishna Yadav**, Department of Mechanical Engineering, Indian Institute of Technology (IIT) Indore, for their invaluable guidance, encouragement, and unwavering support throughout the entire project process. I have been fortunate to have supervisors who cared so much about my work and promptly responded to my questions and queries. Their expertise and insightful suggestions have been instrumental in shaping this thesis.

My heartfelt gratitude to my seniors, lab mates, and colleague researchers, especially **Mr. Dnyanesh Mirikar, Mr. Rajat Kumar, Mr. Zen Kapadiya and Mr. Dinesh** for their cooperation and stay to make M.Tech. project journey happy and joyful.

I am indebted to my family for their constant love, understanding, and encouragement. Their unwavering belief in my abilities has been my greatest motivation.

Finally, I am thankful to all who directly or indirectly contributed, helped, and supported me.

Janupala Chakradhar Reddy
(Roll No.: 2202103034)

ABSTRACT

An experimental investigation is carried out using particle image velocimetry (PIV) and infrared thermography to study the flow dynamics and heat transfer behavior. The orifice configurations studied are single-circular, single-oval, multi-circular, multi-oval, and mixed (circular + oval). The single-oval has higher vorticity levels in the near-field region (Z/D<2) compared to the single-circular due to axis-switching phenomena. While the reduction in the vorticity level is gradual in single-orifice configurations, multi-orifice configurations retain it up to Z/D~8, and a sudden decrease is observed. Oval-shaped orifices produced more turbulence near-field region (Z/D~2), this results in a superior heat transfer performance in oval-shaped orifices at Z/D=2. In comparison to single-orifice configuration, the multi-orifice configurations show a greater rate of entrainment in the near-field of the orifice exit (Z/D<2). The normal stress contours of multi-orifice jets near the orifice exit are thicker and wider, indicating higher turbulence than single-orifice jets, though this turbulence cannot be sustained over longer axial distances. Notably, multi-oval orifices exhibit higher centerline velocities, while single-circular and single-oval orifices demonstrate lower centerline velocities. The single-circular spreads more after Z/D=7, while the multi-orifice spread is larger in the near-field region (Z/D~2). A ~29 % increment in average Nusselt number is observed in multi-oval configuration than in single-circular. The mixed-orifice configuration shows similar characteristics to that of oval-shaped at lower Z/D, while at higher Z/D to that of circular. These findings contribute to a comprehensive understanding of the flow dynamics in synthetic jets with various orifice configurations, offering valuable insights for applications in enhanced mixing and thermal management applications.

Keywords: Synthetic jet, Heat Transfer, PIV, Nusselt Number, Turbulence.

TABLE OF CONTENT

	Page No.
ACKNOWLEDGEMENT	iii
ABSTRACT	iv
TABLE OF CONTENT	v
LIST OF FIGURES	vii
LIST OF TABLES	ix
NOMENCLATURE & ABBREVIATIONS	1
Chapter 1 Introduction	2
1.1 Background	2
1.2 Design and configuration of SJ	3
1.3 Parameters impacting SJ characteristics	4
1.4 Applications of SJ	6
1.5 Brief literature review	8
1.6 Research gap	9
Chapter 2 Literature Review	11
2.1. Orifice shape	11
2.2 Frequency of actuation or excitation frequency	12
2.3 Heat transfer characteristics of multi orifice	13
2.4 Dimensionless parameters	15
2.5 Effects of orifice edges on the performance of a SJ	16
Chapter 3 Investigation and Data Processing Experimental	17
3.1 Background overview	17
3.2 Orifice configurations	18
3.3 Flow measurement setup and procedure for PIV measurements	19
3.4 Data processing and coordinate system in this PIV investigation	21
3.5 Heat transfer setup	22
3.6 Mathematical Formulation	24
Chapter 4 Results and Discussions	27
4.1 Flow characteristics of SJ orifice	27
4.2 Distribution of the vorticity for SJ	28
4.3 Distribution of a normal stress (V_{rms})	30

4.4 Distribution of a Reynold stress for SJ 32
4.5 Mass flow rate 34
4.6 Jet centerline velocity 35
4.7 Jet half-width 36
4.8 Heat transfer characteristics of SJ 36
4.9 Heat transfer characteristics of single orifice SJ 37
4.10 Heat transfer characteristics of multi-orifice SJ 38
4.11 Heat transfer characteristics of mixed-orifice SJ 39
Chapter 5 Conclusions and Scope of Future Work 41
5.1 Conclusions 41
5.2 Scope of future work 42
References 44

LIST OF FIGURES

Fig No.	Figure Captions	Page No.
1.1	Illustration of the operational sequence of a synthetic jet (a) suction stroke, (b) ejection stroke of vortices and (c) vortex ring propagates way from the orifice	4
1.2	Synthetic jet (a) instantaneous and (b) time-averaged	4
1.3	Parameters influencing the formation of synthetic jet	5
1.4	Laptop microprocessor cooling using jet	6
1.5	(a)Synthetic jet directed on aerofoil for flow control (b) Manipulating airflow patterns using Synthetic jet	7
1.6	(a)Synthetic jets can be directed on an electric motor in an EV (b) Electric motor	7
2.1	Heat transfer characteristics of different orifice shapes by (a) L.D Mangate.et.al [45] and (b) Bhapkar et al.[41]	12
2.2	Instantaneous flow field of an impinging SJ at (a) (low Sr=0.03) (left) and (b) (High Sr=0.43)(right)	13
2.3	Variation of Nu_{avg} for different z/d at two different SJ	14
2.4	Variation of Nu_{avg} for four different orifice configurations	14
2.5	Variation of Nu_{avg} with surface spacing for different values of pitch circle radius for the 5×3×4 configuration at Re=2600	15
2.6	Orifice edge configuration(a)Flat, (b)Round and (c) Cusp used by Lee et al.	16
3.1	Single orifices plates and configurations for PIV measurements (a) SC and (b) SE	17
3.2	Multi orifices and mixed orifice plates and configurations for PIV measurements(a) C-CC-8S, (b) M-CC-(4C-4HE)S and (c) E-VC-(4H-4V)S	18
3.3	The experiment setup employed for the PIV measurement	21
3.4	Illustration of the coordinates system used for PIV	22
3.5	Experimental setup of synthetic jet cooling	24

3.6	Heat loss from the heating plate surface due to other modes than forced convection due to impinging synthetic jet	26
4.1	Mean velocity vector field superimposed with velocity contour for circular and oval orifices	29
4.2	Mean velocity vector field superimposed with velocity contour for multi-circular, multi-oval and circular-oval orifices	30
4.3	Mean velocity vector field superimposed with V_{rms}(normal stress) contour for circular and oval orifices	31
4.4	Mean velocity vector field superimposed with V_{rms}(normal stress) contour for multi-circular, multi-oval and circular-oval orifices.	32
4.5	Mean velocity vector field superimposed with Reynold stress contour for circular and oval orifices	33
4.6	Mean velocity vector field superimposed with Reynold stress contour for multi-circular, multi-oval and circular-oval orifices	34
4.7	Variation of the mass flow rate of orifices along the axis of the synthetic jet. (a) Till Z/D =6 (b) Till Z/D = 12	35
4.8	Variation of Jet centerline velocities of orifices along the axis of the synthetic jet	36
4.9	Variation of Jet half width of orifices along the axis of the synthetic jet	37
4.10	Variation of the Nu_{avg} with orifice-to-plate spacing for single-orifice configuration	38
4.11	Variation of Nu_{avg} with orifice-to-plate spacing for single-circular and Multi-circular configurations	39
4.12(a)	Variation of the Nu_{avg} with orifice-to-plate spacing for multi-circular and multi-oval configurations	40
4.12(b)	Variation of the Nu_{avg} with orifice-to-plate spacing single, multi and mixed-orifice configurations	40

LIST OF TABLES

Table no.	Table Captions	Page No.
3.1	Orifice configurations with notations	18
3.2	Specifications of different orifice plates	19

NOMENCLATURE AND ABBREVIATIONS

d	Diameter of center orifice (mm)
d’	Diameter of circular satellite orifice (mm)
f	Diaphragm oscillation frequency (Hz)
H	Cavity depth (mm)
z	Axial distance between the heated copper block and orifice plate (mm)
z/d	Normalized axial distance
T	Period of diaphragm oscillation cycle (s)
t	Time (s)
U_o	Time-averaged jet-blowing velocity over the entire cycle (m/s)
u	Instantaneous jet exit velocity (m/s)
x	Axial coordinate measured from the orifice exit (mm)
v	Molecular kinematic viscosity (m^2/s)
T_s	Surface temperature (°C)
T_a	Ambient temperature (°C)
Nu	Nusselt number
Nu_{avg}	Average Nusselt number
SJ	Synthetic jet
SJA	Synthetic jet actuator
HWA	Hot wire anemometer
AR	Aspect ratio
PCR	Pitch circle radius
Re	Reynolds Number
Sr	Strouhal number

Chapter 1

Introduction

1.1 Background

Thermal management and heat dissipation are critical aspects across diverse industrial sectors, from automotive engineering to electronics manufacturing. In the automotive domain, conventional cooling methods for internal combustion engines often rely on fins and radiator fans. Meanwhile, the rapid proliferation of VLSI and microelectronics in the electronics industry has led to densely packed circuits that challenge traditional cooling techniques due to space limitations. To address the demand for high heat dissipation rates in compact spaces, researchers have explored alternative cooling strategies beyond conventional approaches like radiator fans, thermosyphons[1], microchannels[2-3], and thermoelectric coolers [4].

The operational activity of various electronic components, including processors, memory modules, power electronics, and computer servers, leads to heat generation. Synthetic jet (SJ) technology is employed as a cooling mechanism to address these thermal challenges. According to J. Stephen Campbell *et al.* [5], the microjets led to an average 26% decrease in temperature rise, outperforming under natural convection conditions. There are many applications in addition to their role in thermal management[6-9]. In electric motor thermal management, SJ technology presents a compelling solution to address heat dissipation challenges within the stator and rotor windings. The ability to deliver targeted and controlled airflow directly onto critical motor components makes SJs well-suited for optimizing thermal performance and enhancing overall efficiency. Strategically positioning SJs near the stator and rotor windings makes it feasible to implement localized cooling that effectively mitigates thermal hotspots. The oscillatory nature of SJs facilitates the efficient removal of heat from these crucial motor elements, thereby improving operational reliability and extending the motor's lifespan.

The direct application of SJs for electric motor cooling offers several advantages over conventional methods. Unlike bulky cooling systems that may require complex installations or compromise the compactness of motor designs, SJs can be integrated into the motor housing with minimal impact on overall size and weight. This adaptability is particularly advantageous for electric vehicles, where space optimization and weight reduction are key priorities. Moreover, SJ cooling enables precise control over airflow parameters, such as frequency and velocity, allowing for tailored cooling profiles to specific motor operating conditions. This flexibility enhances thermal regulation and maintains optimal motor performance across varying load and temperature scenarios.

1.2 Design and configuration of SJ

SJ technology has emerged as a promising solution. SJs, also referred to as "zero-net-mass-flux" (ZNMF) jets[10-12], operate without the need for external fluid supplies. Instead, these jets are driven by an oscillating diaphragm or actuator, creating a periodic movement in the surrounding fluid, as seen in Figures 1.1 and 1.2. During the intake phase, the diaphragm moves away from the orifice, enlarging the cavity and lowering its internal pressure. This decrease in pressure induces surrounding fluid to flow into the cavity. Conversely, in the expulsion phase, the diaphragm pushes fluid out through the orifice, generating vortex rings that propagate away from the source. As the diaphragm undergoes periodic oscillation, any vortex rings or pairs shed during the previous ejection phase move sufficiently away from the orifice, remaining unaffected by the inflowing fluid. These results in the downstream generation of non-zero momentum attributed to the diaphragm's rhythmic motion. Consequently, the continuous diaphragm oscillation initiates a sequence of coherent vortex rings within the fluid system. These vortex rings effectively transfer momentum to the surrounding fluid without adding mass. Over time, the vortex rings transform, rolling, coalescing, and developing radial instability, eventually transitioning into a turbulent flow state.

This innovative approach simplifies operational requirements and enhances system adaptability and efficiency, making SJs an attractive option for various fluid dynamics applications. SJ generation utilizes diverse vibrating membrane technologies, reflecting a broad spectrum of innovative approaches. One category involves mechanical drivers, as explored by researchers such as Cater *et al.* [11], who have investigated methods employing mechanical oscillators. Another technique utilizes electromagnetic principles, as Chaudhari *et al.* [13] demonstrated in 2010, showcasing the use of electromagnetic actuators to induce fluid movement. Piezoelectric systems, exemplified by the work of Mane *et al.* [14], offer a distinct avenue for generating SJs by applying piezoelectric materials. Additionally, researchers like Paolillo *et al.* [15] in 2017 have explored acoustic mechanisms, leveraging sound waves to create SJs. This diverse range of membrane technologies underscores the adaptability and versatility of SJ generation methods across different research studies and practical applications, highlighting the innovative nature of fluid dynamics research.

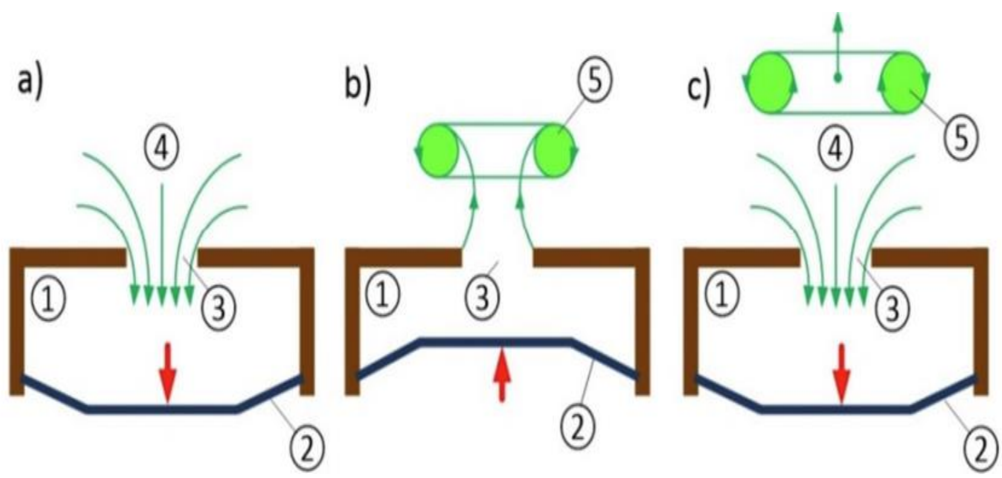

Figure 1.1: Illustration of the operational sequence of SJ a) suction stroke, b) ejection stroke of vortices and c) vortex ring propagates away from orifice ① cavity, ② diaphragm, ③ orifice, ④ ingested fluid, ⑤ vortex ring [12]

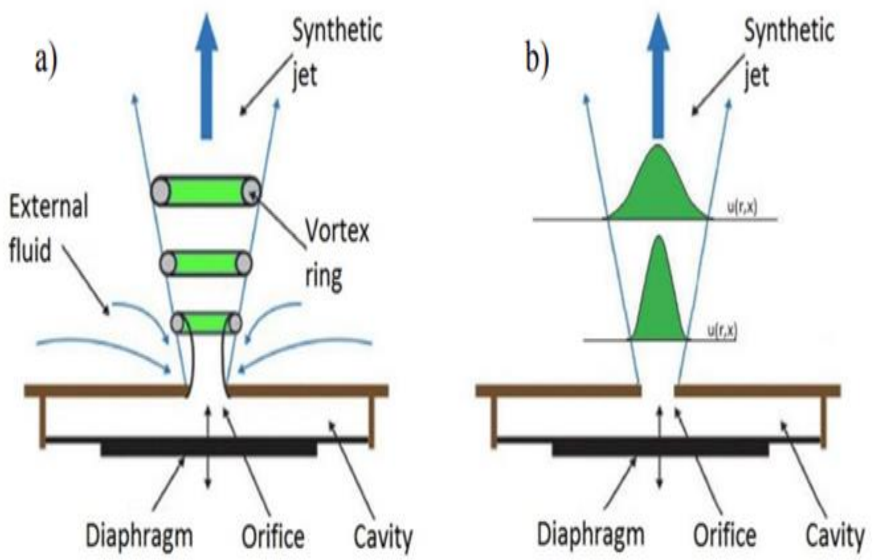

Figure 1.2: SJ (a) instantaneous and (b) time-averaged [12]

1.3 Parameters impacting SJ characteristics

Various factors play crucial roles in influencing the formation and characteristics of SJs, as shown in Figure 1.3 [16, 17]. These parameters influence a wide range of variables that impact the performance and effectiveness of SJ systems. Some of the key parameters include

1.) Actuation Frequency: The actuation frequency of the diaphragm's oscillation directly determines the rate at which fluid is ejected and suctioned through the orifice, influencing vortex formation and fluid dynamics.

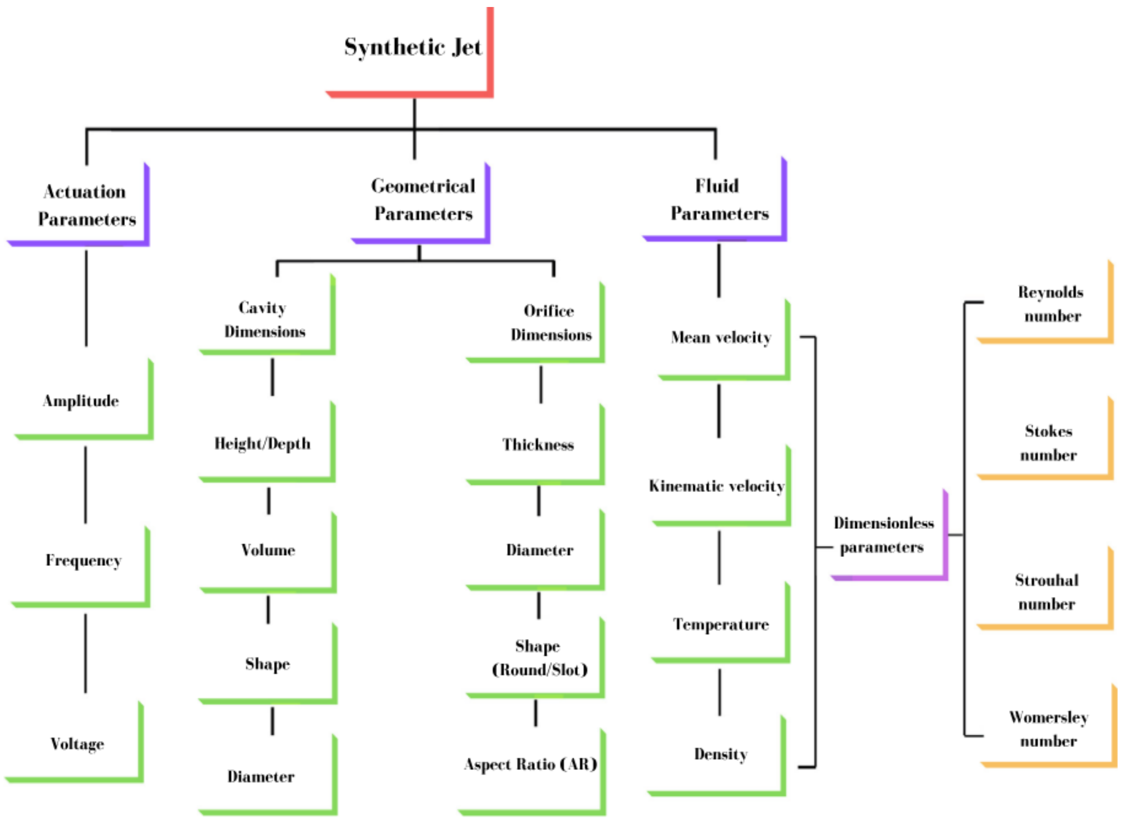

Figure 1.3: Parameters influencing the formation of SJ [16, 17]

2.) The Strouhal number (Sr), which considers the excitation frequency, orifice diameter, and exit velocity, measures how these factors collectively affect the flow characteristics of SJs. Pavlova *et al.* [18] have studied the impact of excitation frequency (e.g., 420 Hz and 1200 Hz) on SJ cooling performance. They found that at lower orifice-to-surface distances ($z/d < 10$), high-frequency jets (e.g., 1200 Hz) exhibit superior heat dissipation compared to low-frequency jets. Conversely, at higher distances ($z/d > 15$), low-frequency jets (e.g., 420 Hz) demonstrate enhanced heat dissipation relative to high-frequency jets.

3.) Orifice geometry:

The orifice's size, shape, and configuration significantly influence the flow pattern, velocity profile, and the formation of vortex structures during the ejection phase of SJs. Multi-orifice SJs often exhibit enhanced heat transfer characteristics at lower surface spacings, while single-orifice shapes like circular or slot configurations demonstrate higher heat transfer efficiency at larger surface spacings. This underscores the critical impact of orifice geometry on the performance and effectiveness of SJ cooling.

4.) Fluid Properties:

The fluid properties, including viscosity and density, play a pivotal role in shaping the behavior and dynamics of fluid flow within the SJ system. Viscous fluids can dampen oscillations and affect the jet's stability, while fluid density influences the momentum transfer and efficiency of heat transfer processes. Optimizing fluid properties is essential for enhancing the thermal performance of SJs in various applications.

1.4 **Applications of SJ**

SJs have various applications across different industries and fields due to their unique capabilities and advantages. Here are some typical applications of SJs:

(i) Electronic cooling

SJ air cooling has emerged as a highly effective method for cooling test chips and laptop processors[19]. This approach positions a series of micro jets directly over the laptop processor. Each microjet operates using a closed electromagnetic actuator to generate airflow. This closed system alternately draws in and expels air based on the input signal frequency of the microjet. To prevent recirculation and enhance cooling efficiency, baffles are strategically placed to direct the airflow in a controlled manner. Compared to natural convection cooling methods, these SJs achieve a remarkable 30 percent higher heat transfer rate, demonstrating their effectiveness in dissipating heat from electronic components, as shown in Figure 1.4. Similarly, numerous researchers have studied electronic cooling using SJ technology [20-23]. These investigations have explored the effectiveness of SJs in dissipating heat from electronic components, such as microprocessors and integrated circuits, by varying orifice geometry and operating conditions.

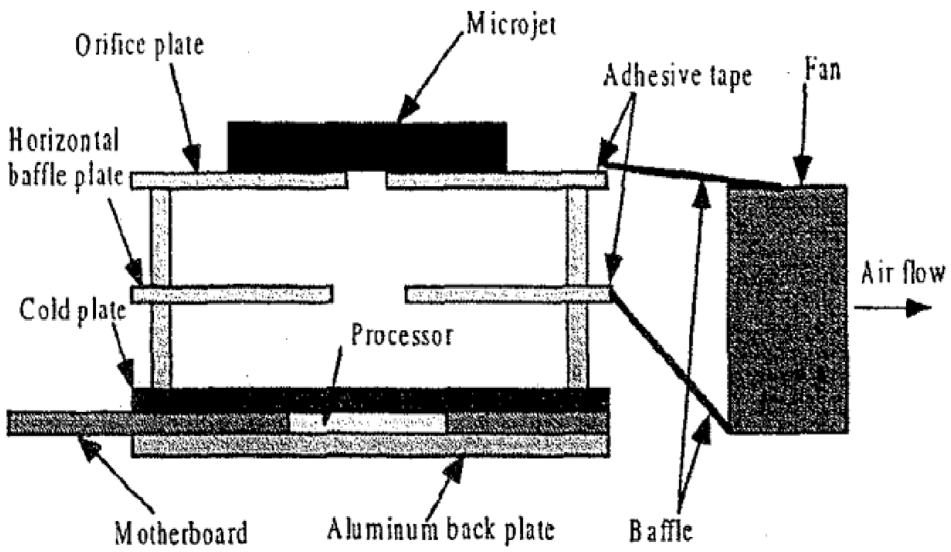

Figure 1.4: Laptop microprocessor cooling using jet[19]

(ii) Aerospace and aviation

SJs are employed in aircraft to control the boundary layer, which is the thin air layer adjacent to the wings' surface or other aerodynamic surfaces. By injecting SJs into the boundary layer, it is possible to modify the airflow and prevent separation or stall at high angles of attack, as shown in Figure 1.5. This technology helps maintain smooth and efficient airflow over the aircraft's surfaces, improving overall aerodynamic performance [24]. In aerospace engineering [25-27], SJs are utilized for active flow control. By strategically deploying SJs at specific locations on the aircraft's surfaces, engineers can manipulate airflow patterns to optimize lift, reduce drag, and enhance control authority. This active control mechanism allows for adaptive aerodynamic configurations tailored to different flight conditions, improving overall efficiency and performance.

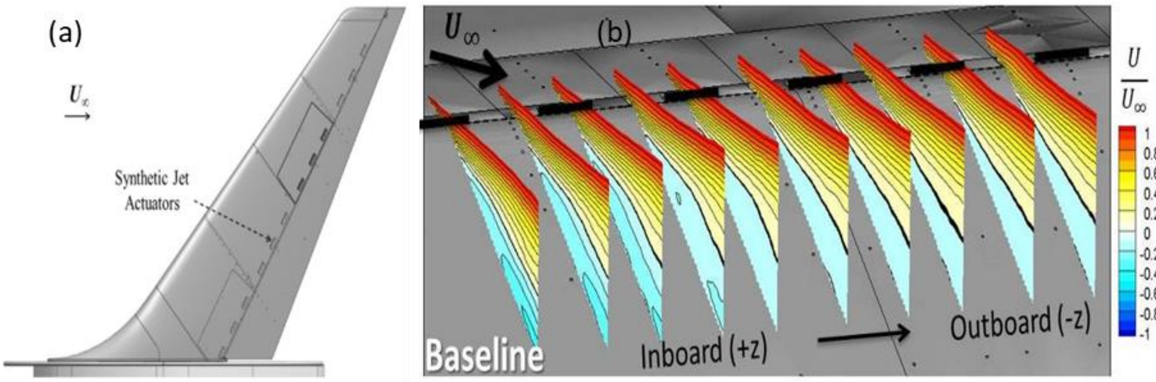

Figure 1.5: (a) SJ directed on aerofoil for flow control and
(b) Manipulating airflow patterns using Synthetic jet[25-27]

Likewise, there are many applications in automotive engineering to reduce vehicle drag and enhance thermal management to prevent overheating, as we can direct the SJ onto the electric motor in Electric vehicles, as in Figure 1.6. Similarly, SJs are employed in industrial processes for fluid mixing[28-31], dispersion of particles, and enhancing chemical reactions. They can achieve efficient fluid control and optimize process efficiency in various manufacturing applications.

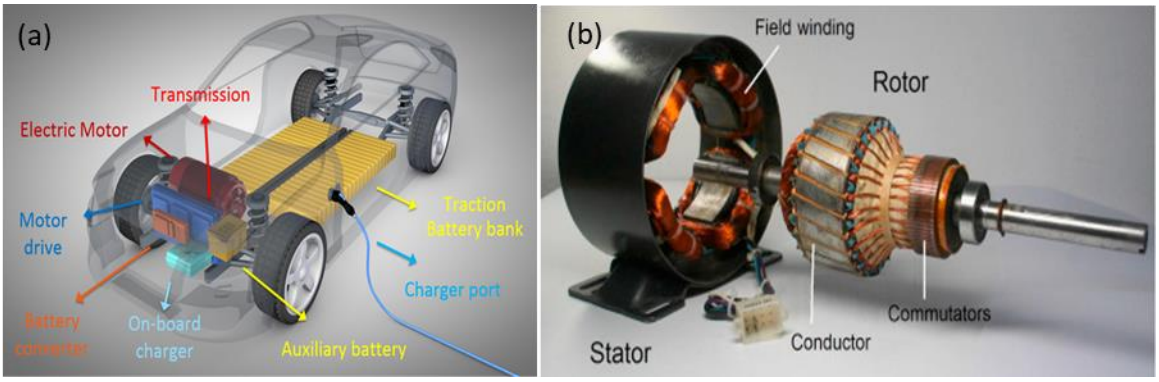

Figure 1.6: (a) SJs can be directed on electric motors in electric vehicles and

(b) Electric Motor

1.5 Brief literature review

The first synthetic jet actuator (SJA) was developed by Dauphinee in 1957, initially referred to as an air-jet generator used in laboratory settings [32]. Subsequent advancements in SJ technology have been driven by three primary parameters that enhance heat transfer: actuation, fluidic, and geometric [33]. The diaphragm's orifice shape and operating frequency impact flow characteristics more. Because of its extensive use, the dynamics of fluid movement and heat transfer patterns produced by an SJ by a single orifice and multi-orifice have gained significant interest. The characteristics of the SJ orifice are contingent upon diverse factors, including actuation parameters, fluid properties, and geometric considerations, as detailed by Gopal Krishan et al. [34]. In conclusion, the study on the effects of geometric parameters on SJs, as outlined by Mun Hoh Hong et al. [35], reveals critical insights into the intricate dynamics of SJ flow fields. The three distinct flow regimes, namely near-field, transitional, and far-field regions, elucidate the complex interplay of discrete vortex rings and their impact on the overall performance of SJs. Geometric parameters, such as orifice shape, aspect ratio, orifice depth, and cavity height, play pivotal roles in shaping the characteristics of SJs. In earlier investigations into continuous jets, researchers such as Gutmark *et al.* [36] and Wang *et al.* (2018)[37] delved into the impact of orifice shape on flow and heat transfer characteristics. Michalke's et al. [38] work in 1971 contributed to the observation that noncircular (asymmetric) jets exhibit a natural predisposition toward greater instability compared to circular (axisymmetric) jets. This inherent instability in noncircular jets results in greater mixing capabilities, distinguishing them from their more stable circular counterparts. Notably, the axis-switching phenomenon in noncircular orifices and the optimal aspect ratio for maximizing time-averaged velocity underscore the relationships between geometry and performance.

The study of heat transfer characteristics of single orifice SJ and the effect of various parameters such as variation of average heat transfer with orifice diameter, cavity depth, and thickness of orifice plate are discussed in Chaudhari et al. [39] saying, the orifice diameter proves to be a crucial factor, showcasing a direct correlation with the average heat transfer coefficient, which increases as the orifice plate thickness decreases. Cavity depth, on the other hand, exerts a negligible impact on heat transfer. The cavity's resonance frequency emerges as a pivotal point, with the maximum average heat transfer coefficient aligning with this frequency. Wang *et al.* [40] investigated the impact of aspect ratio on elliptical and rectangular SJs (aspect ratios 3 and 5) using particle image velocimetry. Their study demonstrated that the initial axis switching in elliptical orifices is nearer to the jet orifice than in rectangular orifices. The effect of single orifice shapes such as circular, elliptical, rectangular, square, etc., on mean flow characteristics such as velocity vectors, vorticity, and normal stress are discussed in Bhapkar *et al.* [41] stated that the vortices generated in the wall jet by the elliptical orifice possess greater energy compared to the vortices produced by other orifice shapes mentioned above. Still, Chaudhari *et al.* [42] discovered a notable 30% increase in heat transfer rate for a multi-orifice SJ as opposed to a single orifice SJ when subjected to equivalent input power for small surface spacings, i.e., $z/d<2$. The distance of the surface from the SJ orifice emerges as a crucial factor influencing heat transfer variations. Notably, the SJ's effectiveness has diminished at smaller surface spacings due to the concurrent suction and ejection of the same fluid. Addressing this concern, Bhapkar *et al.* [42] delved into the impact of various cavity shapes on resulting heat transfer rates. Their findings underscore an intriguing pattern: circular orifices exhibit diminished heat transfer rates at reduced surface spacings compared to their oval counterparts. In contrast, circular orifices surpass oval shapes in heat transfer rates as surface spacings increase. This was also demonstrated by Lee *et al.* [43]; the reason for axisymmetric jets like circular ones to have larger heat transfer rates at higher Z/D is the phenomenon is ascribed to the substantial loss of momentum in the central region of the elliptic jet before reaching the impingement plate. This loss is attributed to a larger entrainment and stronger mixing with the ambient fluid. They observed that the elliptical jet exhibited a 15% higher heat transfer rate than its circular counterpart under conditions of a small nozzle-to-plate spacing. Intriguingly, this trend reversed when confronted with a larger nozzle-to-plate spacing, indicating a nuanced dependency of heat transfer performance on aspect ratio and spatial configurations.

1.6 Research gap

The existing literature underscores the significant influence of orifice shape, orifice-to-plate distance, and flow dynamics on heat transfer characteristics. Notably, multi-orifice configurations exhibit enhanced heat transfer rates at lower orifice-to-plate distances than their single-orifice counterparts. This observation has inclined research interest in various multi-orifice setups, but those with a central orifice and satellite orifices of similar shapes. It is essential to recognize the distinct advantages of different orifice shapes, such as oval orifices excelling at shorter distances and circular orifices demonstrating superior performance at greater distances. Hence, a study with a circular and oval integrated orifice called a mixed orifice shape with circular at the center and oval and circular as satellite orifices has yet to be done. This literature review highlights the need for a comprehensive investigation into the flow characteristics of mixed orifice shapes and oriented multi-orifice configurations, a gap the current study aims to address. Multiple openings' arrangement, orientation, and positioning significantly influence the flow patterns and heat transfer properties. It is imperative to conduct thorough investigations into these aspects to comprehend their impact effectively.

The overarching goal of this research paper is to pinpoint an orifice configuration that demonstrates characteristics reminiscent of an oval at lower z/d ratios while transitioning towards circular characteristics at higher z/d ratios. In pursuit of this objective, an examination of flow characteristics, mass entrainment, vorticity contours, mean velocity vectors, jet width, and more has been conducted across various orifice configurations, encompassing multiple and mixed shapes involving oval and circular geometries.

- **Chapter 1:** Provides an overview of SJs, exploring their diverse applications. It concisely reviews relevant literature and outlines the study's objectives.
- **Chapter 2:** An extensive literature review is conducted to provide a detailed understanding of how different parameters influence SJ behavior.
- **Chapter 3:** Here, we delve deeper into experimental investigations, encompassing the setup of particle image velocimetry (PIV) and heat transfer experiments. The focus is exploring single- and multi-orifice SJ configurations' flow characteristics and heat transfer properties.
- **Chapter 4:** Provides a comprehensive elaboration of the results obtained from the experimental investigations, offering detailed insights and analysis.
- **Chapter 5:** It delves into the conclusions drawn from our current experimental inquiries. This chapter also explores the potential for future research in this area.

Chapter 2

Literature Review

Over the decades, numerous studies have explored the intricacies of SJs, particularly emphasizing key parameters that affect their performance. Geometric considerations, such as the shape and size of orifices, have been scrutinized for their impact on jet behavior and efficiency. Researchers have investigated how parameter variations alter the jet's flow structure and resultant heat transfer capabilities. Moreover, the frequency of actuation and excitation frequencies play a pivotal role in determining the efficacy of SJs. Studies have investigated optimal frequencies to achieve desired flow characteristics and heat transfer rates, balancing the need for effective jet formation with minimal energy consumption.

The spacing between orifice outlets and nearby surfaces is another critical parameter that has garnered attention in the literature. This spacing can influence the development and stability of SJs, impacting their ability to enhance heat transfer and fluid mixing in different applications. Reynolds number (Re) and Sr are fundamental parameters governing the dynamics of SJs. These dimensionless numbers characterize the flow regime and shedding frequency within the jet system, providing insights into its operational behavior and performance across varying conditions. By delving into this literature, researchers have gained valuable insights into optimizing SJ design and operation for enhanced flow control and heat transfer applications. This foundational knowledge serves as a springboard for further investigations into advanced jet configurations and novel applications within fluid dynamics and thermal management.

2.1 Orifice shape

The shape of the orifice has a notable impact on heat transfer rates from surfaces, as shown in Figure 2.1. Studies by Gutmark *et al.* [36] and Wang *et al.* [37] demonstrate that asymmetric jets, like oval or rectangular shapes, induce greater mass entrainment and fluid mixing compared to axisymmetric jets. This enhanced mixing significantly affects heat transfer characteristics, especially at shorter distances between the orifice and the plate. In their research, Wang *et al.* [37] utilized stereoscopic particle image velocimetry to investigate elliptical and rectangular SJs with aspect ratios of 3 and 5. They observed that the first axis switching for the elliptical orifice occurs closer to the jet orifice than the rectangular orifice. Zaman *et al.* [44] examined the spreading characteristics of free jets from asymmetric nozzles and rectangular orifices across Mach numbers ranging from 0.3

to 2.0. The study concluded that elliptical and rectangular nozzles exhibit higher spreading rates than circular nozzles in the supersonic regime. Bhapkar *et al.* [41] and L. D. Mangate *et al.* [45] investigated how different cavity shapes affect heat transfer rates. They discovered an interesting trend: Circular orifices showed lower heat transfer rates at shorter surface spacings than oval shapes. However, circular orifices outperformed oval shapes in terms of heat transfer efficiency with increased surface spacings.

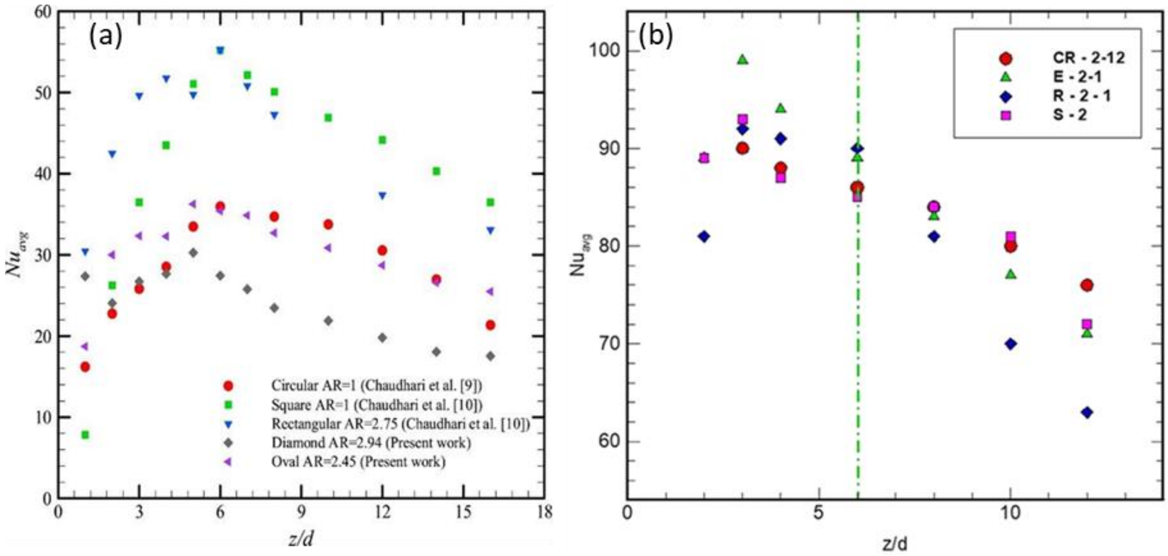

Figure 2.1: Heat transfer characteristics of different orifice shapes by (a) L.D Mangate.et.al [45] and (b) Bhapkar et al.[41]

2.2 Frequency of actuation or excitation frequency

The influence of excitation frequency is often linked with low-frequency jets; individual vortex rings impinge on the surface due to the large wavelengths between coherent structures Pavlova et al. [18]. Conversely, vortex rings tend to separate with high-frequency jets and then merge back together. Vejrazka *et al.* [46] investigated the impact of excitation frequency corresponding to Sr=0.2-4 and Re=10,000 at a low surface distance (z/d=2). They observed that low-frequency excitation led to the formation of larger vortices compared to cases without excitation. The transition between these two distinct behaviors occurred at approximately Sr=0.25.

As per the findings of Sharma *et al.* [47], as shown in Figure 2.2, the SJ flow field at a low Sr=0.03 is characterized by primary vortex rings followed by a trailing jet. In this scenario, each vortex ring impacts the surface individually due to the significant wavelength between coherent structures. In contrast, at a high Sr=0.43, the jet flow field demonstrates a sequence of primary vortices that accumulate and undergo fragmentation into smaller structures before reaching the surface. At high Sr values, the jet exhibits a notable 17.5% increase in average Nusselt number (Nu_{avg}) compared to a low Sr jet, as shown in Figure 2.3.

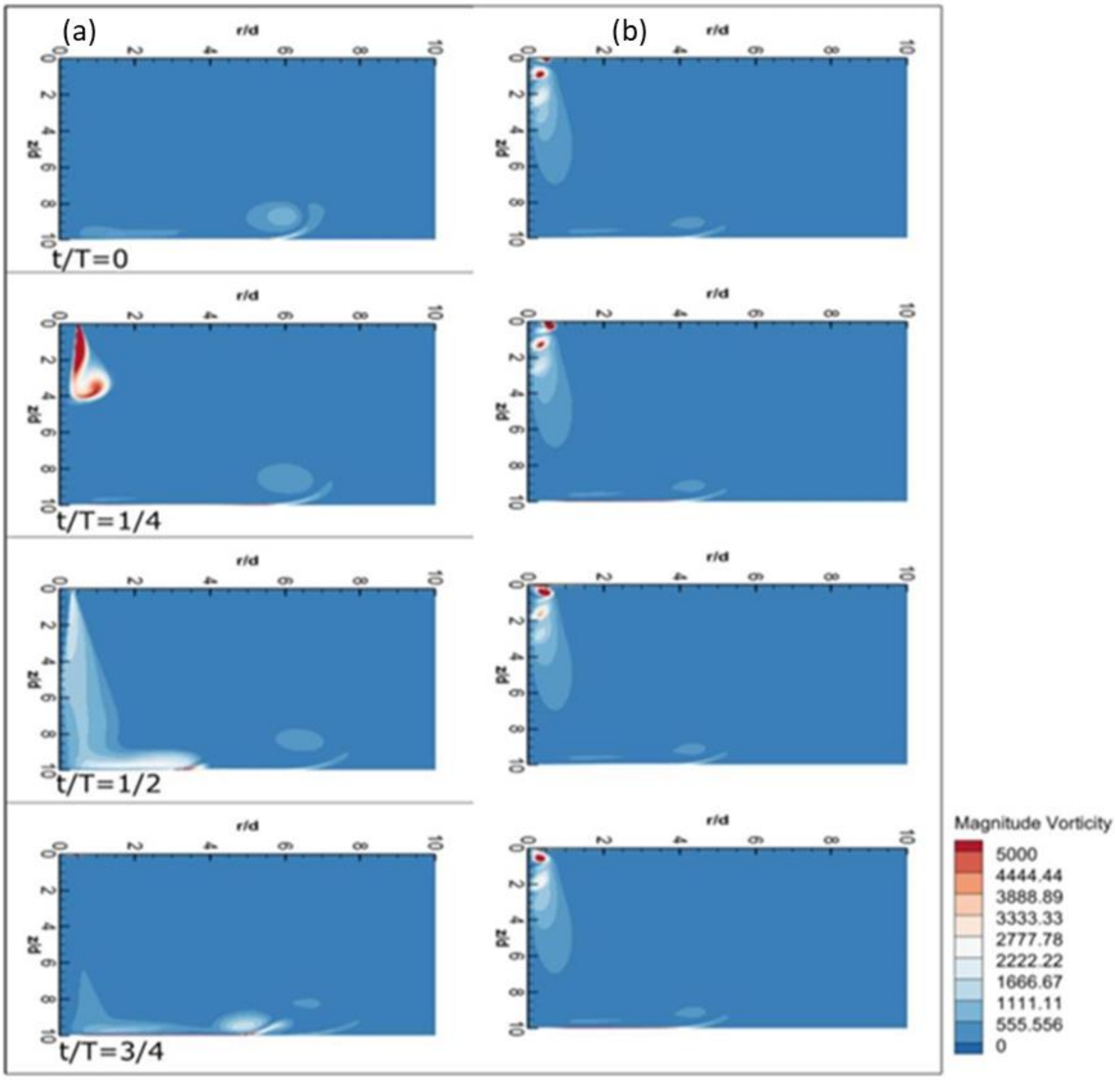

Figure 2.2: Instantaneous flow field of an impinging SJ at (a) low Sr=0.03 and (b) high Sr=0.43 [47]

2.3 Heat transfer characteristics of Multi orifice

In multi-orifice configurations, a central orifice is surrounded by satellite orifices. Research by Harekrishna Yadav *et al.* [48] and Chaudhari *et al.* [45] explores various arrangements of orifice plates, such as (5×3×2), (5×3×4), and (5×3×8), to form multi-orifice jets. For example, in a 5×3×2 configuration (illustrated in Figure 2.4), the numbers 5 mm and 3 mm denote the diameters of the central and surrounding satellite orifices, respectively, with 2 representing the number of satellite orifices.

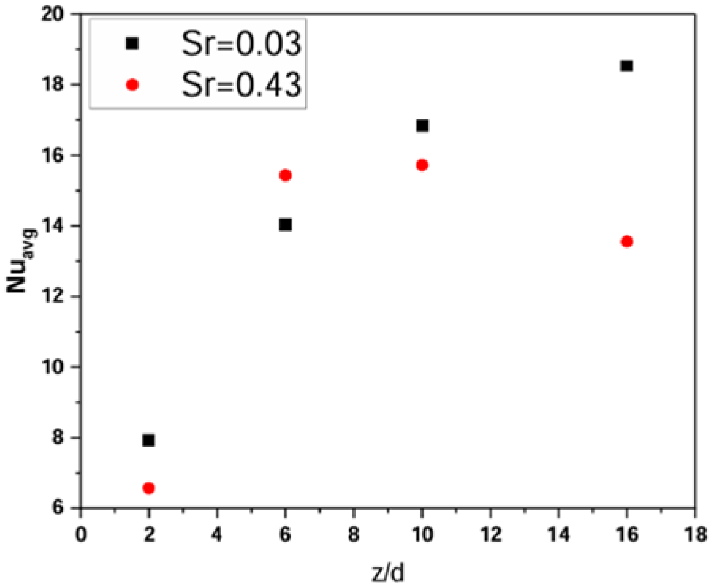

Figure 2.3: Plots for Nu_{avg} as a function of z/d at two different Sr jets.[47]

The studies indicate that multi-orifice configurations exhibit higher heat transfer coefficients than single-orifice setups (5 mm and 8 mm). Specifically, for single orifice and 5×3×8 configurations, the heat transfer coefficient gradually increases, reaches a maximum value, and decreases. In contrast, multi-orifice configurations (such as 5×3×1, 5×3×2, and 5×3×4) show two distinct peaks in the heat transfer coefficient: one at a lower surface spacing (z/d=2) and another at larger spacings as shown in Figure 2.4. The pitch circle radius (PCR) of satellite orifices also influences the heat transfer characteristics, as seen in Figure 2.5.

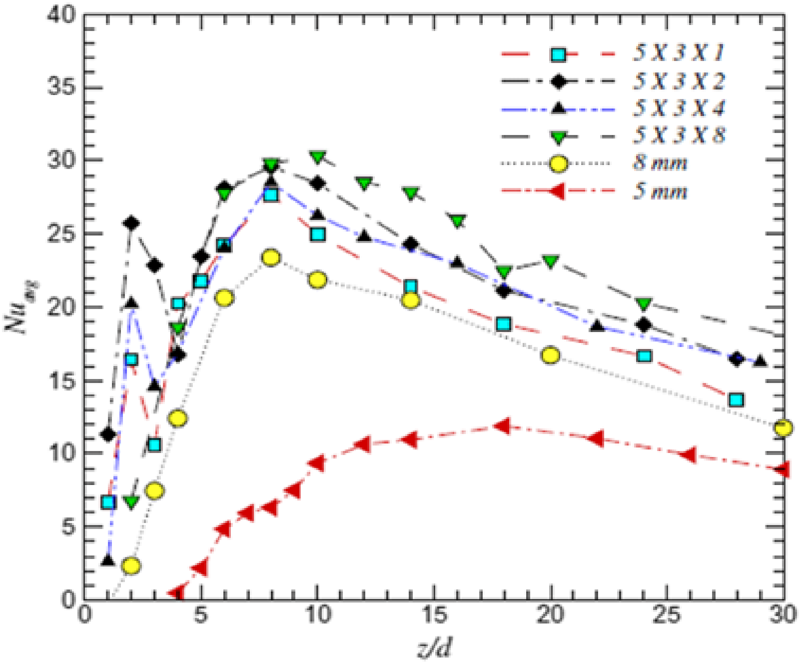

Figure 2.4: Nu_{avg} versus z/d for various orifice configurations[45][48]

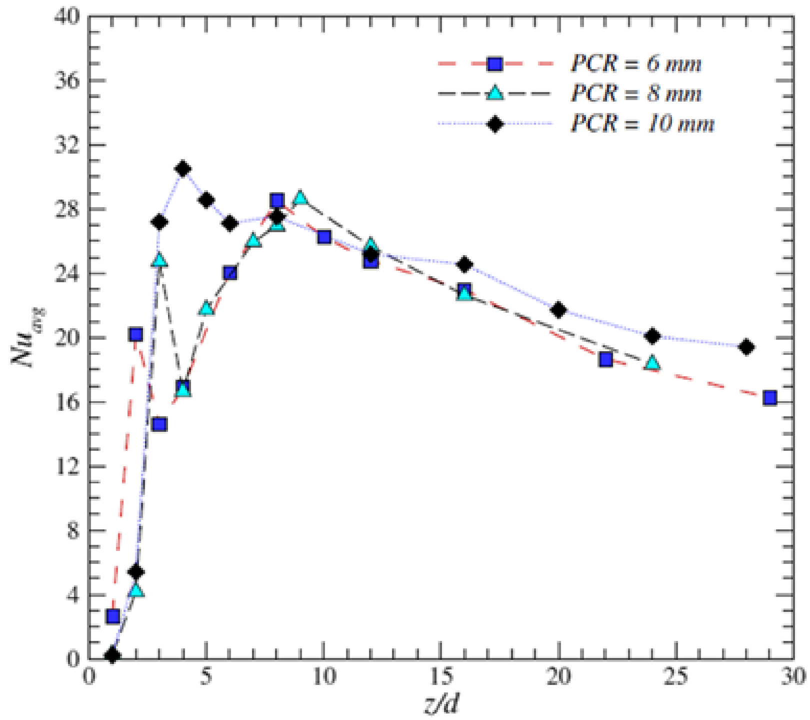

Figure 2.5**:** Nu_{avg} for different pitch circle radius (PCR) values for 5×3×4 configuration at Re = 2600.[45][48]

At smaller spacing ratios (z/d<2), the central jets have insufficient time to develop fully. As a result, the satellite jets are not influenced or drawn towards the central jet, leading to separate jet impingement on the surface.

2.4 Effect of stroke length (Lo) and Reynolds number (Re)

The effects of stroke length and Re on heat transfer in SJs can be significant and can be used in various engineering applications. The stroke length of a SJ refers to the distance the jet travels during each oscillation cycle. In terms of heat transfer, a longer stroke length can potentially enhance heat transfer by increasing fluid mixing near the surface. This improved mixing can help disrupt the boundary layer and promote convective heat transfer. However, excessively long stroke lengths may lead to inefficient energy usage or even flow separation, hindering heat transfer effectiveness. According to Rylatt *et al.* [49], at a constant Re of 2000, When the jet is more confined ($L_o/D=40$)(Stroke length), it experiences greater confinement by the surrounding walls of the duct. This confinement can restrict the expansion of the jet, reducing its ability to mix with the surrounding fluid. As a result, the heat transfer is limited compared to the less confined jet ($L_o/D=18$), where there is more space for the jet to expand and mix with the surrounding fluid, promoting better heat transfer. In the stagnation region, where the jet impinges directly onto the surface, the confined jet ($L_o/D=40$) may experience higher pressure gradients and reduced mixing than the less confined jet ($L_o/D=18$). This can lead to a lower heat transfer rate for the more confined jet in the stagnation region.

2.5 Effects of orifice edges on the performance of a SJ

Conventionally, most SJAs have sharp-edged orifices. Researchers like MH. Hong *et al.* [35] have conducted comparative studies to investigate how different edge configurations (such as bevel, round, and cusp shapes) impact the characteristics of the jet velocity and effectiveness of the jet. Lee *et al.* [50] conducted a numerical study focusing on 2D slotted orifice edges in SJs, as shown in Figure 2.6. They compared three types of orifice edges: flat, round, and cusp shapes under specific conditions, including a constant Re of 104.2 and stroke ratio of 15.9, where Re and stroke length are based on the slot half-width (w). The rounded edge configuration exhibited a lower peak streamwise velocity than the flat edge case, ~20% lower. This difference was attributed to the rounded edge's ability to prevent flow separation, thereby restricting the constriction effect through the slot.

The rounded edge configuration was observed to entrain or expel more fluids during the ingestion and expulsion phases of the SJ operation. This increased fluid movement contributed to a higher spanwise velocity than the flat edge case. Overall, the findings suggest that the shape of the orifice edge in SJs significantly influences jet characteristics and effectiveness. The rounded edge configuration promotes smoother flow behavior by minimizing flow separation, enhancing fluid movement and altering the SJ's velocity profiles.

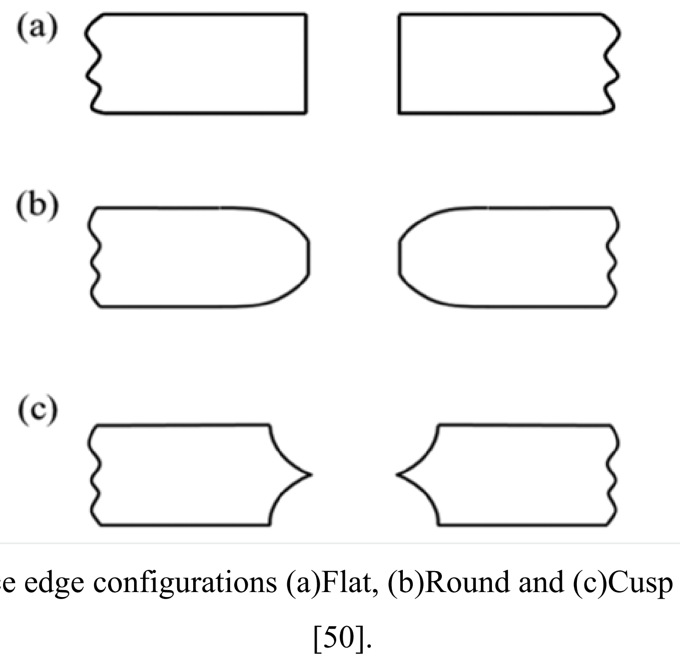

Figure 2.6: Orifice edge configurations (a)Flat, (b)Round and (c)Cusp used by Lee *et al.* [50].

Chapter 3

Experimental Investigation and Data Processing

3.1 Experimental setup overview

This section provides an in-depth overview of PIV and outlines the setup for conducting velocimetry measurements. These measurements are instrumental in analyzing the flow physics of various orifice configurations, including single-orifice, multi-orifice, and mixed-orifice shapes, as illustrated in Figures 3.1 and 3.2. PIV plays a pivotal role as an optical method to understand how SJs behave in fluid flow. This technique precisely measures the speed and direction of fluid movement by monitoring the movement of tiny tracer particles suspended in the flowing fluid. Extracting vital information about the fluid involves using a CCD digital camera with PIV to capture images of these tracer particles randomly dispersed in the flow at different time intervals.

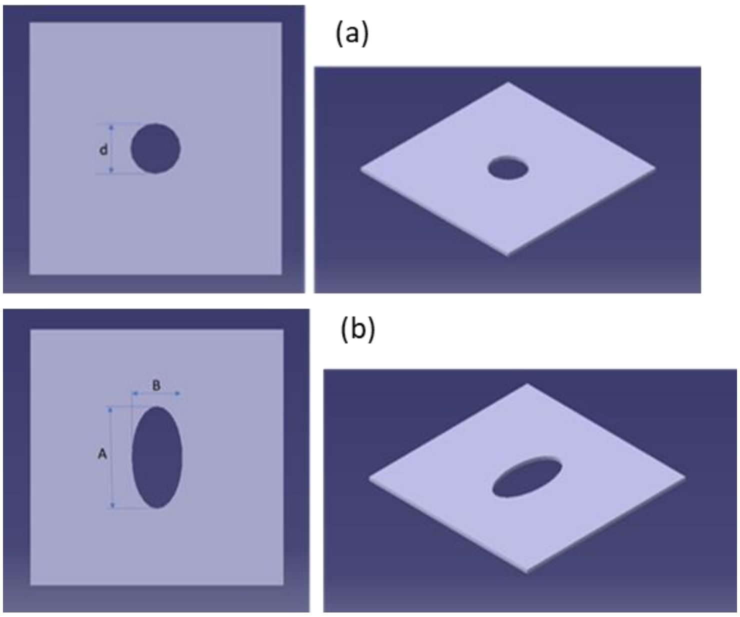

Figure 3.1: Single orifices plates (a) SC and (b) SE configurations for PIV measurements

Through this process, we obtain crucial details about the fluid's dynamics and behavior. PIV recordings are generated by synchronizing intense laser light flashes with the CCD camera's image capture process. As particles move within the flow, they become illuminated upon passing through the laser sheet plane. A single CCD camera then captures the light scattered by these particles. The laser flash, lasting approximately 10 nanoseconds, induces scattered light from the particles, which travels through the camera lens and reaches a photosensitive sensor inside the CCD camera. This sensor typically comprises a grid of small light-sensitive elements known as pixels arranged in a square or rectangular array. In the digital recordings, the images of these particles present themselves as distinct bright spots. These images are further segregated into pairs of frames, which are subsequently analyzed by data acquisition and processing software, as detailed by Raffel *et al.* [51].

3.2 Orifice configurations

Various orifice plate configurations facilitate accurate and detailed flow measurements, as shown in Figures 3.1 and 3.2. Table 3.1 gives the orifice configurations with notations.

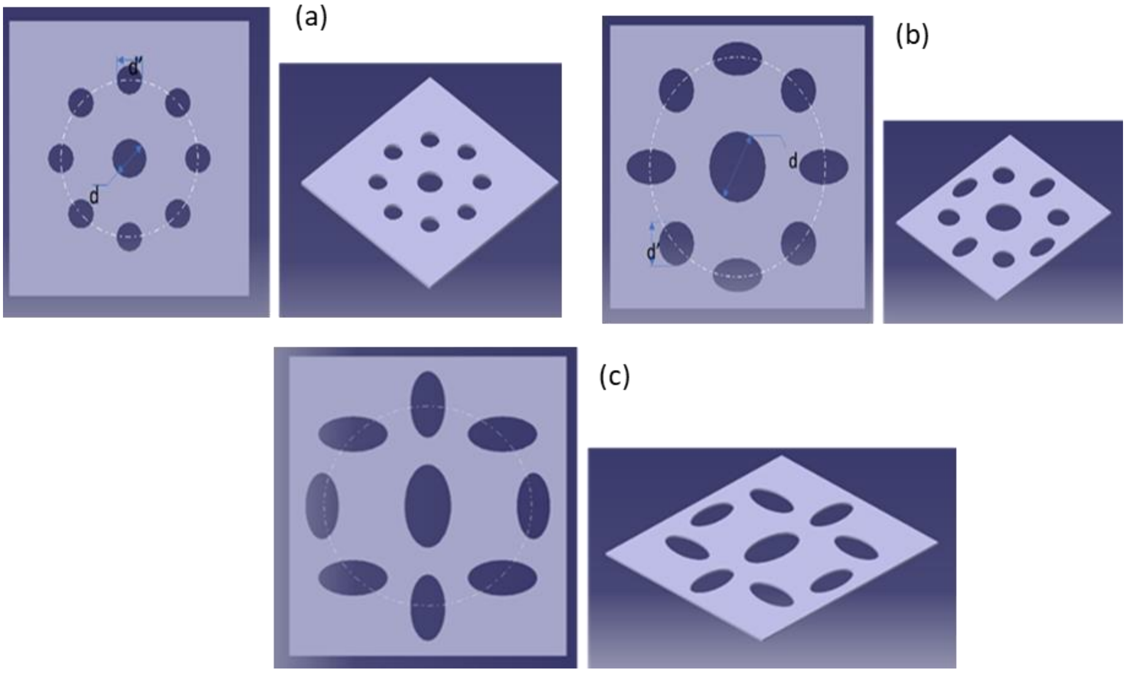

Figure 3.2: Multi and mixed orifices plates and configurations (a) C-CC-8S, (b) M-CC-(4C-4HE)S and (c) E-VC-(4H-4V)S for PIV measurements

Table 3.1: Orifice configurations with notations

Single orifice:	
SC	Single circular
SE	Single oval
Multi-orifice:	
C-CC-**8**S	All orifices are circular, having 8 satellite orifices
M-CC-(**4**C-**4**HE)S	Mixed orifices have circular orifices at the center, 4 circular satellite orifices, and 4 elliptical orifices with major horizontal axes.
E-VC-(**4**H-**4**V)S	All elliptical orifices have a major axis vertical ellipse at the center; 4 satellite orifices have a major axis horizontal, and the other 4 have a major axis vertical.

Table 3. 2 Specifications of different orifice plates:

Orifice	Shape	Aspect ratio (AR)	Dimensions (in mm)
SC	Circular	1	d=10
SE	Oval	2	A=14.14, B=7.07
C-CC-8S	Multi-Circular	1	d=5, d'=3.06
E-VC-(4H-4V)S	Multi-oval	2	A=7.06, B=3.54; a=4.33, b=2.17
M-CC-(4C-4HE)S	Mixed-orifice (Circular-Oval)	2	A=7.06, B=3.54; a=4.33, b=2.17; d'=3.06

3.3 Flow measurement setup and procedure for PIV measurements

The experimental arrangement includes a transparent flow chamber with dimensions of 50×50×50 cm^3, crafted from a see-through material like glass, as shown in Figure 3.3. At the top of the flow chamber, an acoustic speaker, integrated with an orifice plate, is securely mounted. Within the flow chamber, tracer particles are present and introduced through a seeding generator. The PIV study utilized a 70 mm speaker, and the single orifice jet had a diameter of 10 mm. Additionally, the hydraulic diameter for all multi-orifice and mixed-orifice configurations, as shown in Figure 3.2, was maintained at 10 mm. To achieve the periodic suction and expulsion of air in the form of a jet, the vibrating membrane of the SJ operated at its resonance frequency. A function generator regulates the vibrations of the speaker's diaphragm. A function generator is an electronic device that produces various waveforms at controlled frequencies, such as sine, square, or triangular waves. It precisely controls the frequency of the input power to the speaker, ensuring the desired oscillations for the SJ system. The oscillations, diaphragm amplitude, and resonance frequency were determined according to the specifications provided by U. S. Bhapkar *et al.* [42] and M. Chaudhari *et al.* [52]. A Tektronix TDS 2022B function generator was employed, setting the frequency at 80 Hz and the voltage at 4 V for all orifice configurations specified in Figure 3.2. The resonance frequency was determined through hot-wire anemometry (TSI, IFA300)-based measurements. A solitary normal probe, crafted from tungsten and featuring a probe length of 1.27 mm and a diameter of 4 µm, is strategically placed perpendicular to the speaker. This probe determines the maximum velocity by varying frequencies. It is positioned at a distance of 0.25 cm from the speaker. The resulting data aids in identifying the resonance frequency associated with the maximum velocity. Additional insights into the Hot-Wire Anemometry (HWA) method can be explored in the works of Bhapkar *et al.*

[52], Chaudhari *et al.* [42], and S.G. Mallinson *et al.* [53]. These references provide comprehensive details and methodologies for applying HWA in the context of the current study.

The expelled air from the orifice is directed into the flow chamber or test section, and its momentary velocity vectors are visualized using seeding particles introduced by a seeding generator. To generate fine particles in the 1-2 μm[54], atomizer chambers containing liquids like olive or vegetable oil leverage the open jet pump principle. An oil particle generator enriches the airflow within the flow chamber with oil particles. The detailed working seeding generator and its dependency are detailed in Raffel *et al.* [51], Adrian *et al.* [55], Bhapkar *et al.* [52], and Yadav *et al.* [48].

Utilizing Nd: YAG pulsed lasers (Vlite-700, Beamtech, China), we generate a sheet of light using specially designed light sheet optics that incorporate cylindrical and spherical lenses. This carefully crafted light sheet illuminates tracer particles as they pass through its path. The laser system operates at an energy output of 200mJ per pulse, emitting light at a wavelength of 532 nm. Each laser pulse has a duration of 7.7ns and 6.8ns [56], ensuring precision in capturing the desired flow visualization data. A CCD digital camera (PCO Pixelfly, Germany) with a resolution of 1024×1392 pixels and a 12-bit CCD is oriented perpendicularly to the plane of the light sheet. The camera, comprised of small array-like elements called pixels, measures the light exposure of each pixel through its pixel grey value. This enables the effective capture of scattered light emitted by illuminated tracer particles. To ensure precise synchronization, a synchronizer unit controls the time delay between laser pulses and the digital camera, ensuring seamless coordination of the laser pulse frequency and camera operation. The time gap between successive laser pulses is finely tuned to 0.09 milliseconds to adapt to the flow velocity. The study meticulously captures 360 pairs of images at a sampling rate of 5 Hz.

The recorded images are processed using MATLAB in conjunction with PIVLAB 1.4. The software utilized for data acquisition and processing employs a method that involves segmenting pairs of frames into small intervals called "interrogation windows." These windows are utilized to compare particle positions across two frames, leading to the derivation of displacement vectors. The software calculates velocity vectors using spatial cross-correlation techniques to leverage the known time interval between frames. This approach follows a dual-step process, employing interrogation window sizes of 64×64 pixel^2 for the first step and 32×32 pixel^2 for the second. Each subsequent interrogation region maintains a consistent 50% overlap. Notably, a minimal portion, less than 5%, of the total vectors were identified as incorrect and flagged during this process.

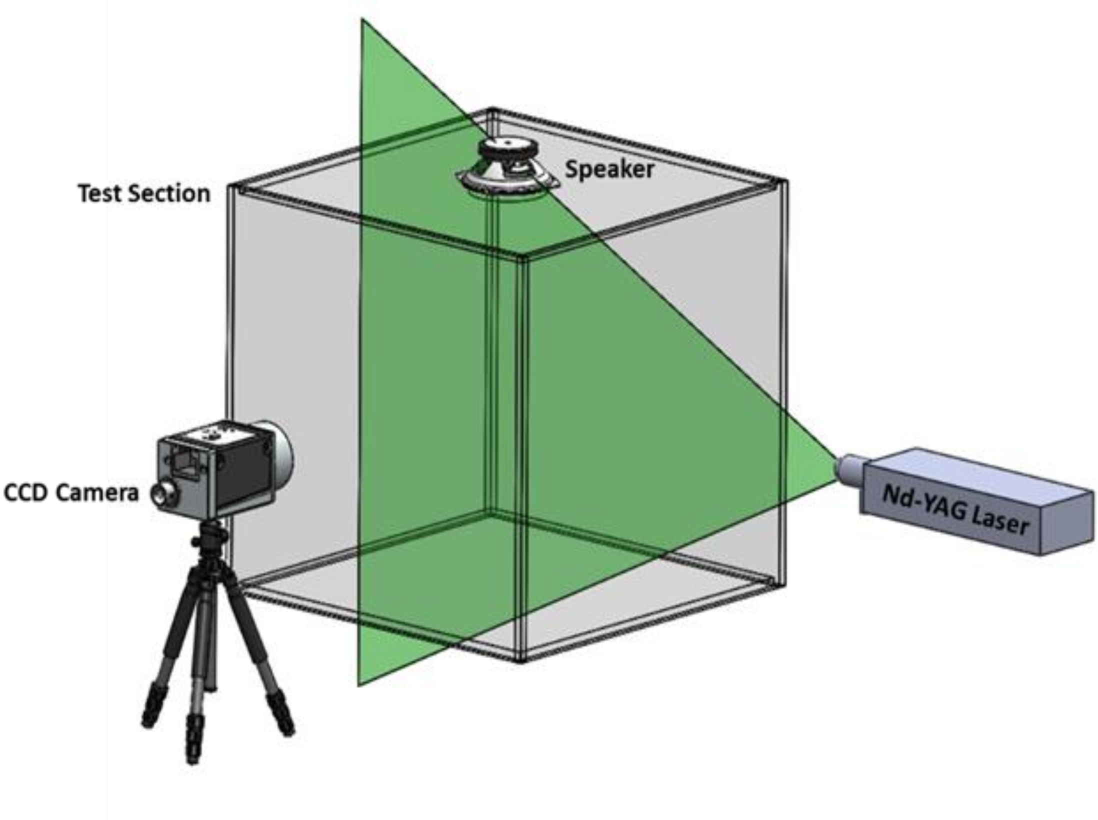

Figure 3.3: Experimental setup employed for the PIV measurements

3.4 Data processing and coordinate system in this PIV investigation

In Figure 3.4, the schematic diagram illustrates the coordinate system employed for PIV measurements, accounting for a speaker size of 70 mm and an orifice hydraulic diameter of 10mm. The z-axis represents the axial direction of the jet, while the r-axis denotes the radial direction. In this representation, the positive direction is considered downward. Vcl denotes the jet centerline velocity, and velocities measured along the axial direction are taken as positive. The orifice exit velocity is determined using Hot Wire Anemometry, as discussed in the Chaudhary et al. section with reference [48].

$$V_0 = L_0 f \tag{3.1}$$

In this context, L0 signifies the length determined across the ejection stroke within a cycle, while f represents the frequency of diaphragm excitation. The Re is then derived based on these specific parameters.

$$Re = \frac{V_0 d_e}{\nu} \tag{3.2}$$

d_e represents the characteristic length or, in this context, the equivalent diameter. The uncertainties in this velocity measurement are calculated based on references [57] and [58-59]. At the proximity of the orifice, the uncertainty is around 12%, and the overall experimental uncertainty for mean velocity is 5.6%.

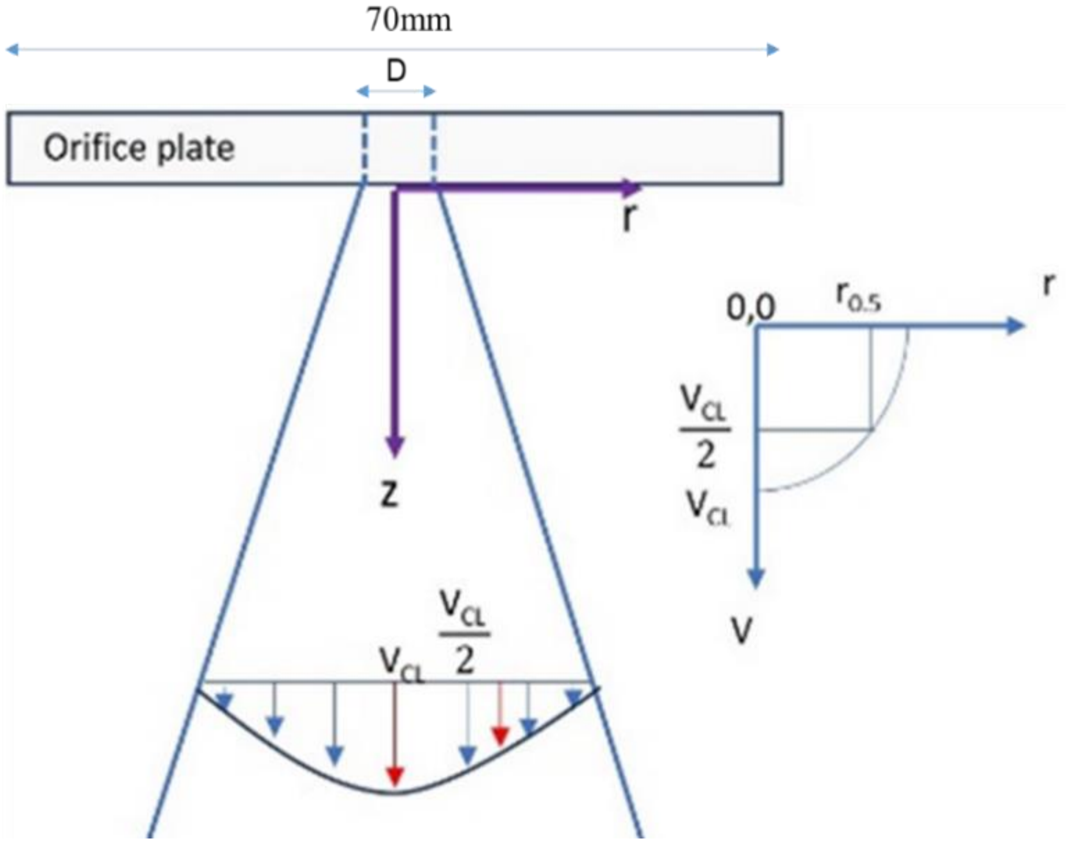

Figure 3.4: Illustration of the coordinate system used for PIV.

3.5 Heat transfer setup

In the heat transfer experiment, as shown in Figure 3.5, a central component is the Visaton FRS 7S speaker, characterized by an 8W rated power, 8 Ω impedance, and an effective piston area of 22 cm^2. This speaker is securely mounted on an acrylic plate measuring 150×150 mm^2 with a thickness of 10 mm. The plate incorporates a bore diameter of 60 mm and a counterbore diameter of 5 mm. Positioned beneath the speaker and acrylic plate of 150×150 mm^2 is an orifice plate crafted from acrylic material, featuring dimensions of 90×90 mm^2 and a thickness of 2.5 mm. This orifice plate is designed to accommodate various orifice shapes, as outlined in Table 3.2, while ensuring a constant opening area for single and multi-orifice jets. For both configurations, the hydraulic diameter remains consistent at 10 mm. This standardized parameter facilitates a controlled comparison between the different orifice shapes and their impact on heat transfer characteristics.

Powering the SJA is the Tiscon SI-28DR power oscillator, directed by a Tektronix AFG1022 arbitrary function generator. The actuator operates at its resonance frequency, determined through a frequency sweep ranging from 80 to 200 Hz, with flow parameters guiding the process. The experimental setup includes measuring various electrical parameters using a Fluke-287 digital multimeter, providing precise readings for DC voltage across the bus bar and AC voltage across the speaker. The multimeter specifications are 0.05–1000 ± 0.025% V for voltage and 0–10 ± 0.05% amp for current. A Meco SMP96 digital panel meter monitors AC voltage across the speaker. This experimental configuration facilitates thoroughly exploring heat transfer characteristics in single and multi-orifice SJs. The study offers valuable insights into the thermal performance implications of different configurations, contributing to our understanding of heat transfer mechanisms in such systems.

In the heat transfer experiment, an SJ generated from the orifice plate is directed onto a test foil made of SS-304 with dimensions of 190×165×0.06 mm^3. This test plate is clamped between two copper bush bars using an M8 nut and bolt mechanism. To ensure emissivity matching, enhance sensitivity, and reduce reflections, the bottom of the plate is coated with black paint. The heating foil is positioned between L-shaped cast iron bars, and to mitigate the risk of short circuits and electrical current leakage, these frames are securely attached to a bakelite plate using nuts and bolts. A constant heat supply is provided to the test foil using a DC power source (GWInstek PSW 30-108). This power source delivers electrical power to the stainless steel plate, acting as the impingement surface. The heat input to the plate directly results from the electrical power supplied, making it crucial for heating experiments or material testing applications. As the electrical power traverses the system, it encounters resistance in the wires connected to the copper bush bar and the DC power source. According to Ohm's Law ($V = I \times R$), where V is voltage, I is current, and R is resistance, the voltage drop across a resistor is directly proportional to the current flowing through it and the resistance itself. A multimeter measures the voltage drop across the copper bush bar. This measurement encompasses the voltage drop due to the resistance in the wires. By measuring the voltage across the bush bar, the effective voltage reaching the impingement surface is captured, accounting for losses in the wires. Once the voltage across the bush bar and the current supplied by the DC power supply are obtained, the power input to the impingement surface can be calculated using the formula $P = V \times I$, where P is power, V is the voltage across the bush bar, and I is the current supplied by the DC power source.

The FLIR-A655sc infrared thermal imaging camera, with a resolution of 640×480 pixels and a sampling frequency of 50 Hz, is strategically positioned 44 cm below the heating surface assembly to capture temperature distribution. The camera ensures detailed thermal imagery operating at a spatial resolution of 0.31 mm/pixel, with each pixel representing a specific area on the heating plate. A minimum temperature differential of 15°C is upheld to maintain accuracy between the heated foil and ambient air. Post-capture, the recorded data undergoes processing using the FLIR Research IR MAX software, equipped with tools for temperature calibration, region-of-interest analysis, and precise temperature measurements. The high sampling frequency of 50 Hz facilitates the capture of dynamic temperature changes, contributing to the camera's effectiveness in applications such as heat distribution monitoring and hotspot identification.

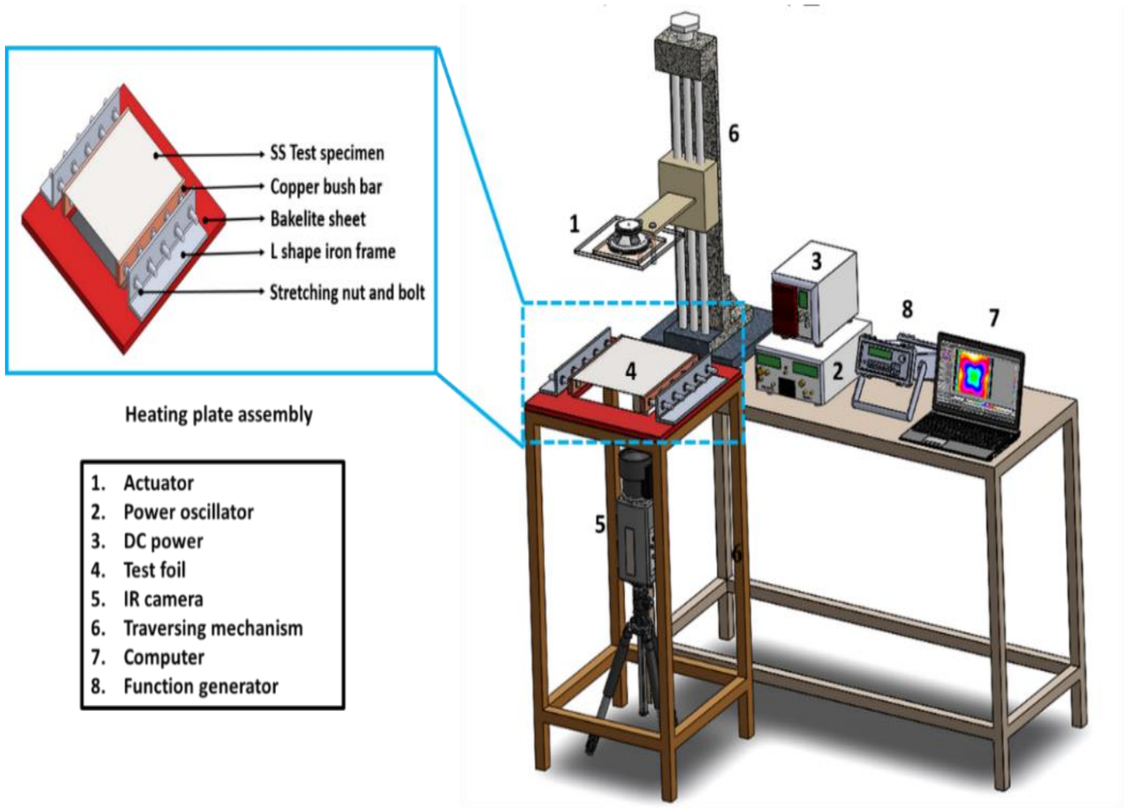

Figure 3.5: Experimental setup of SJ cooling

3.6 Mathematical formulation

A DC power source is used to heat the plate constantly, and the net heat flux supplied to the plate is given by

$$q_{net} = q_s - q_{loss} = \left(V.\frac{I}{A}\right) - (q_{conv} + q_{rad}) \qquad 3.3$$

Where q_s Is the heat flux generated on the foil by the DC power source. q_{loss} Total heat losses due to convection and radiation given by q_{conv} andq_{rad}. An electric current is created when a DC voltage is applied across a resistive foil, such as a heating foil. The foil offers resistance to this current flow, converting the electrical energy into heat according to Joule's law [60]. Using Joule's law and Ohm's law, the amount of heat generated (q_s) per unit of time in the foil can be calculated as

$$q_s = (V \times I) / A \tag{3.4}$$

This heat supplied involves measuring the voltage drop across the copper bush bars and the current flow into the foil. The voltage drop across the copper bush bar refers to the decrease in voltage as electric current passes through it. A voltmeter is used to measure this voltage drop. Connect the voltmeter probes across the copper bush bar to measure the potential difference between two points on the bar. The voltmeter will display the voltage drop across the copper bush bar. The method for determining heat loss is drawn from the research by Sharma et al. [61, 62]. It involves analyzing the temperature differential between the heated surface (represented by T_f) and the surrounding ambient temperature T_a. The SJ from the orifice impinges on the front side of stainless steel foil, which is sufficiently insulated with glass wool. The heat loss equation is given by

$$q_{loss} = 14.07874\left(T_f - T_a\right) + 7.25943 \tag{3.5}$$

Figure 3.6 illustrates the correlation between heat loss and ambient temperature differences. The radiative heat loss originating from the front portion of the specified impinging surface, possessing an emissivity rating of 0.25, is estimated to contribute between 2 to 3% towards the overall heat delivery. In contrast, conduction-driven heat loss, which permeates throughout the heating surface, represents less than 1% of the maximum input heat flux. Considering all factors, the collective heat loss peak is 21.48% of the total heat supplied. This predominant loss stems mainly from natural convective and radiative processes occurring at the rear surface of the impinging foil.

After getting net heat flux, the average heat transfer coefficient (h_{av}e) is found using Newton's law of cooling equation given by

$$q_{net\,=}\, h_{avg}(T_f - T_a) \tag{3.6}$$

After finding out the average heat transfer coefficient, the Nu_{avg} for the jet Impinging on the foil is given by

$$Nu_{avg} = \frac{h_{avg} \cdot d}{k} \tag{3.75}$$

Where d is the characteristic length, k is the thermal conductivity of air.

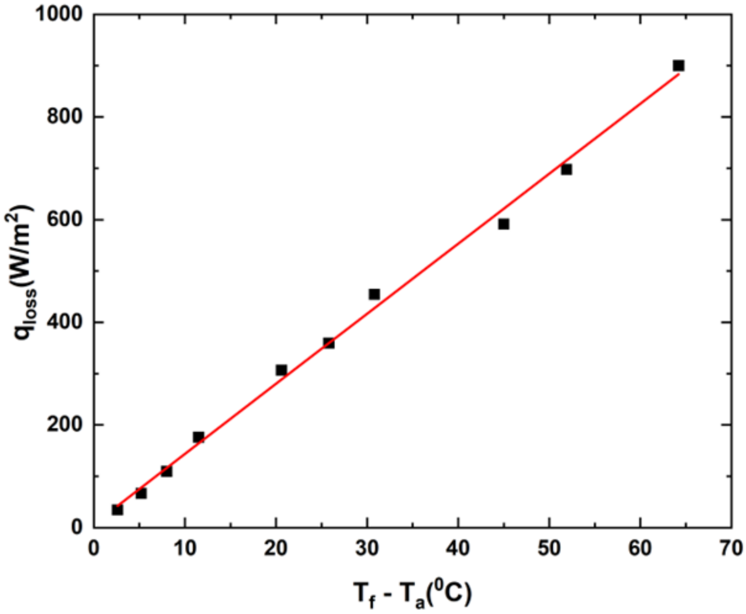

Figure 3.6: Heat loss from the heating plate surface due to other modes than forced convection by impinging SJ

Chapter 4

Results and discussion

The results are divided into two sections: 1st section deals with the flow dynamics around the orifice, and 2nd section deals with the heat transfer characteristics.

4.1 Flow characteristics of SJ orifice

The flow field of the SJ orifice is defined using flow parameters such as vorticity field, mass flow rate, half jet width, centerline velocities (V_{rms}) contour, and Reynold stresses. The half-jet width is typically assessed as a key parameter to quantify the lateral spread of the SJ. This measurement provides insights into the extent to which the jet interacts with the surrounding flow. The half jet width represents the distance from the centerline of the SJ to the point where the velocity reaches half of its maximum value. This measurement is essential for evaluating the jet's spreading characteristics and influence on the surrounding fluid. Determining the half jet width is often conducted through experimental methods like PIV or numerical simulations. Factors influencing the half jet width include the frequency and amplitude of the SJ, the geometry of the orifice or nozzle generating the jet, and the surrounding flow conditions. The mass flow rate in an SJ orifice is a critical parameter that characterizes the amount of mass being expelled or entrained by the SJA. The rate at which mass entrainment happens signifies the performance of mixing and cooling of entrained fluid.

Rms velocities measure the intensity of flow fluctuations and turbulence within the jet, which is crucial for accessing jet stability to mix and interact with the surrounding fluid. It is also used to understand flow physics, such as vortex shedding. Vorticity contours help us understand vorticity strength, quantifying the intensity of rotational motion induced by the fluid by SJ. Vorticity contours can reveal flow separation or recirculation regions within and around the SJ orifice. They help us identify the formation and evolution of vortices within the SJ orifice.

The PIV measurement is conducted for a different office configuration of a single and multi-orifice SJ. The geometric shapes taken are circular, oval, multi-circular, multi-oval, and circular-oval orifices and the reason for taking these orifices is at lower Z/D (orifice to plate distance ratio) oval orifices perform better than single circular orifices and higher Z/D's circular orifice performs better than oval orifice as referred to Bhapkar *et al.* [41].

The idea is to find an orifice that performs better than oval at lower Z/D and better than circular at higher Z/Ds; thus, mixed orifice shapes are taken to achieve this result.

4.2 Distribution of the vorticity for SJ

4.2.1 Single orifice shape

This segment elucidates the mean velocity vector field for singular orifice and multi-orifice jets. The velocity vector field is superimposed with the vorticity contour. Figure 4.1 represents regions with positive vorticity, denoted by red, while a blue hue indicates those with negative vorticity. The color scheme serves as a visual guide, allowing observers to identify the polarity and intensity of vorticity across different areas within the flow field. Figure 4.1 signifies that the vorticity magnitude along the axis of the single circular orifice is lower than the oval orifice at a lower Z/D, i.e., from 0 to 2 oval orifice shows some significant mean vorticity contour compared to a single circular orifice. The reason is that axis-switching phenomena are observed in oval orifices, i.e., a jet emanating from an oval orifice comes out as oval rings, and their axis switches as traveling forward, thereby creating vortical structures in all directions. The shape of an oval orifice can create variations in pressure distributions along its surface, which leads to the development of an adverse pressure gradient due to which flow separation happens on the edge of orifices, which results in the formation of vortices on the wake region by promoting better fluid mixing. As the jet translates along the axis, the circular orifice has a denser vorticity contour than the oval. The oval orifice facilitates the rapid spreading of vortex rings along its minor axis. As the vortex rings undergo a series of contortions, they eventually return to their initial shape, with their axes swapped. This unique behavior significantly boosts the entrainment of ambient fluid and elevates turbulence intensity in near-field regions. This was also observed by Chih-Ming Ho *et al.* [63], who said that the entrainment ratio exhibited by an elliptic jet surpassed that of a circular jet by several multiples. The increased entrainment in the elliptic jet or oval is due to a unique structure that induces distortions, allowing it to pull in large amounts of surrounding fluid. Most of this entrainment happens around the minor-axis plane, where the vortex core moves away from the jet axis, pulling external fluid into the jet stream. This implies that the turbulence characteristics of the elliptic jet are intricately linked to the geometry-induced variations in the shear layer thickness, emphasizing the role of azimuthal distortions in influencing the turbulence dynamics. The observed phenomena collectively underscore the intricate interplay between vortex dynamics, entrainment, and turbulence in the context of small-aspect ratio elliptic jets.

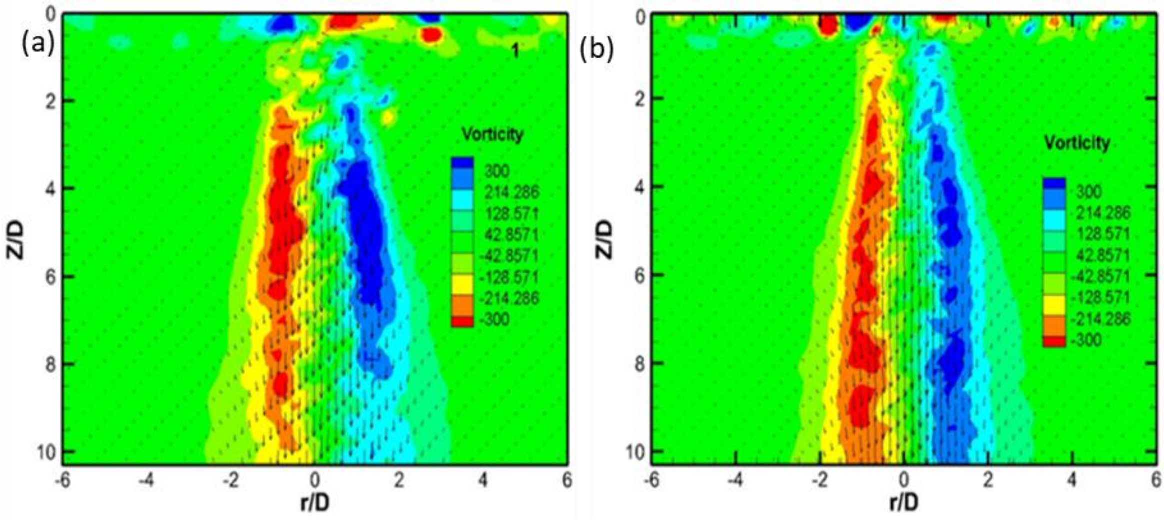

Figure 4.1: Mean velocity vector field superimposed with vorticity contour for (a) circular and (b) oval orifices.

4.2.2 Multi-orifice configuration

Figure 4.2 shows the mean velocity vector field superimposed with the vorticity contour of a multi-circular, multi-oval, and mixed-orifice jet. Comparing single circular and multi-circular orifices, Figure 4.2 signifies the vorticity magnitude along the axis of the single circular orifice is lower than that of the multi-circular orifice and at a lower Z/D. The Z/D of 0 to 2 multi-circular orifice shows some significant mean vorticity contour compared to the single circular orifice. These vorticity contours are thicker, more intense, and translated relatively larger distances than the single orifice vorticity contours. The illustration demonstrates a noteworthy trend in the vorticity contour intensity for the single orifice jet, indicating a gradual decrease up to Z/D≈10. Conversely, the vorticity contour intensity for the multi-orifice jet undergoes a distinct behavior, experiencing a decrease post Z/D≈8. The contour's characteristics reveal a disruption in the vortex emanating from the multi-orifice jet, resulting in a sudden decline in vorticity contour magnitude.

Figure 4.2 shows that the vorticity contours exhibit higher proximity close to the orifice exit, indicating an intensified swirling motion. As the distance downstream increases, these contours have a radial expansion, suggesting a dispersion or spreading out of the rotational flow. At a Z/D~(0 to 2), the vorticity contour of multi-oval is more intense than multi-circular, and the mixed orifice has relatively higher vortices than multi-circular and lower than multi-oval. It is intriguing that as the downstream distance increases, the vorticity contours exhibit a consistent radial expansion for multi-circular, multi-oval, and mixed orifice shapes. The intensity of vorticity contour after (Z/D~8) of circular-oval and multi-oval sustained is relatively larger than a multi-circular orifice. The contour pattern indicates that the swirling motion created by the multi-orifice jet breaks apart after reaching a distance of about Z/D≈8. After this point, there is a gradual decrease in the intensity of the vorticity contour.

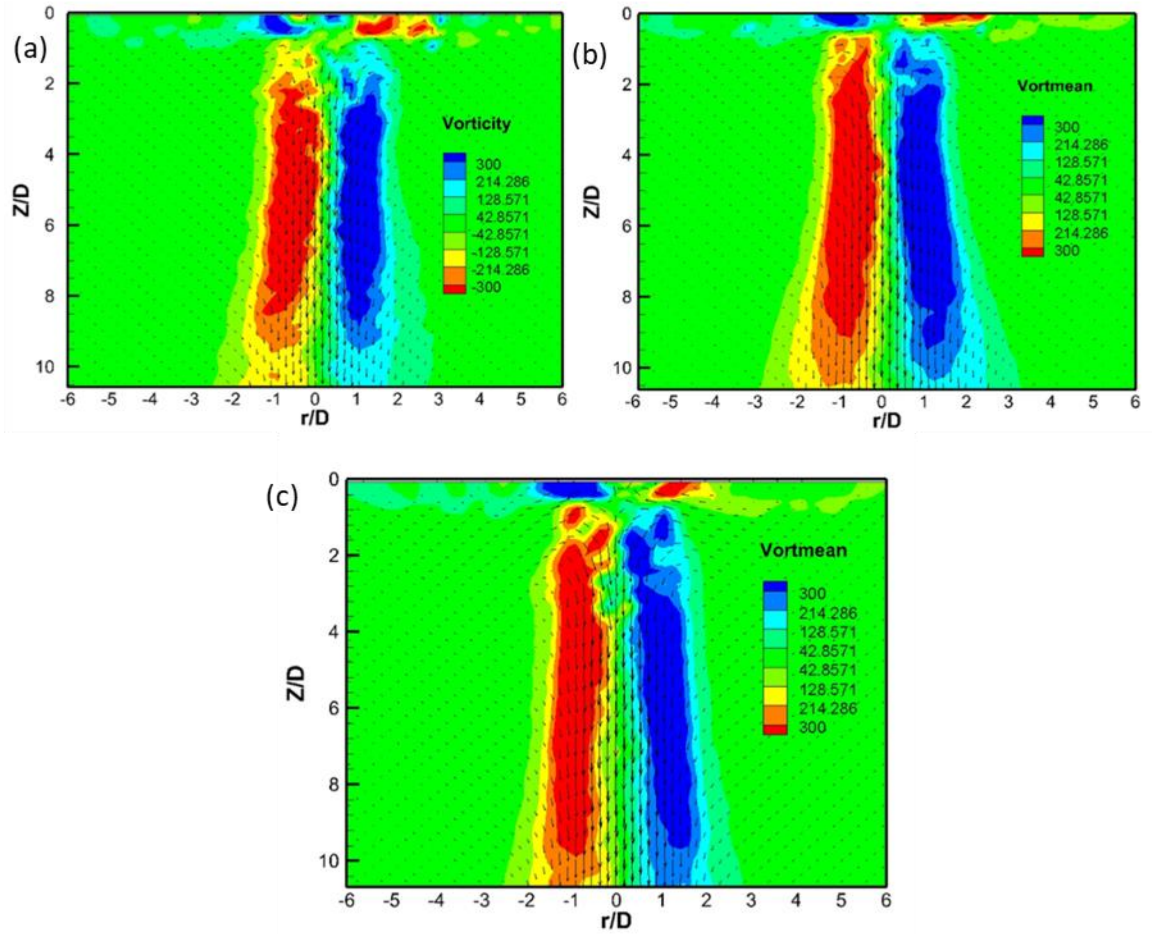

Figure 4.2: Contour of mean velocity vector superimposed with vorticity for (a) multi-circular, (b) multi-oval and (c) circular-oval orifices.

4.3 Distribution of a typical stress (V_{rms}):

4.3.1 Single orifice

This section describes the distribution of the contour of normal stress superimposed on the velocity vector field for both single and multi-orifice shapes. Figure 4.3 shows the normal stress contour for single-circular and oval orifice SJ. In the central jet region, the normal stress exhibits a higher magnitude compared to the shear layer of the jet. Additionally, stress contours gradually expand radially as the axial distance increases. This behavior arises from the ongoing interaction of vortex pairs along the axial direction. Further, the significant values of normal stress persist over an extended axial distance. The stress in the near jet region, i.e., up to (Z/D~2) oval orifice, has significant normal stress due to swirling vortices near the jet orifice compared to circular. In contrast, in the central jet region, the circular orifice sustains larger normal stress intensity axially than the oval orifice up to (Z/D~10) as, for the oval, its intensity reduced drastically after (Z/D~8). Indeed, as previously discussed for oval orifices, the swift switching of axes in the vortex rings occurs at lower axial distances from the orifice exit. This phenomenon contributes to heightened turbulence intensity and increased entrainment of ambient fluid in the vicinity. The dynamic axis switching at shorter distances amplifies the mixing effect, reinforcing the correlation between the orifice's geometry and the fluid dynamics observed in the near-field.

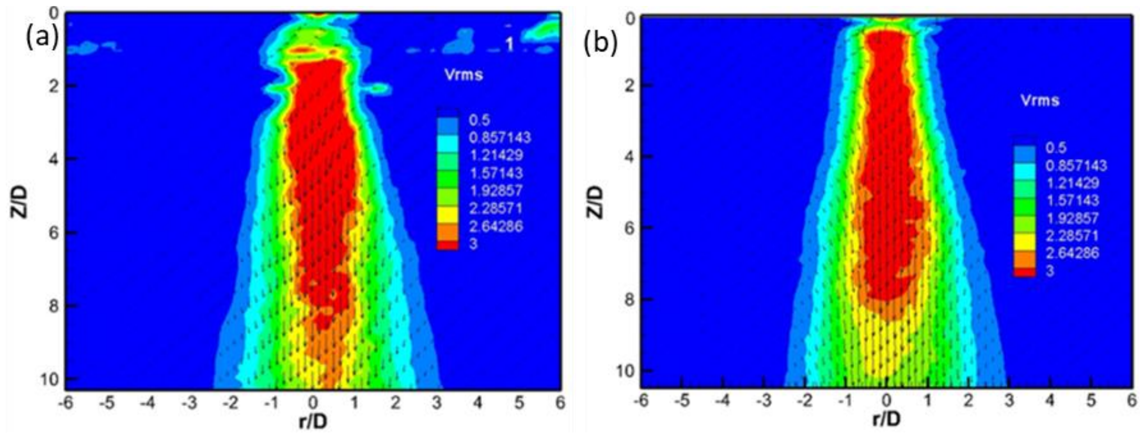

Figure 4.3: Mean velocity vector superimposed with V_{rms} (normal stress) contour for (a) circular and (b) oval orifices.

4.3.2 Multi-orifice and mixed-orifice

Figure 4.4 shows the mean velocity vector field superimposed with the Vrms contour of a multi-circular, multi-oval, and mixed-orifice jet. Comparing these with a single orifice jet, the values in the central jet region have thicker contours. Still, the stress values did not sustain longer distances, and this aligns with our earlier interpretation of vortex interaction, i.e., vortices in a single orifice jet gradually increase in size and endure for a comparatively longer axial distance. In contrast, vortices generated in the multi-orifice jet exhibit larger size and rapid growth along the axial distance and break down eventually after translating to some extent axially. The improved heat transfer rates observed in multi-orifice and mixed orifice configurations compared to single orifices at lower Z/D values can be attributed to heightened turbulence intensity. This characteristic is evident in Figure 4.2, particularly until Z/D<6."

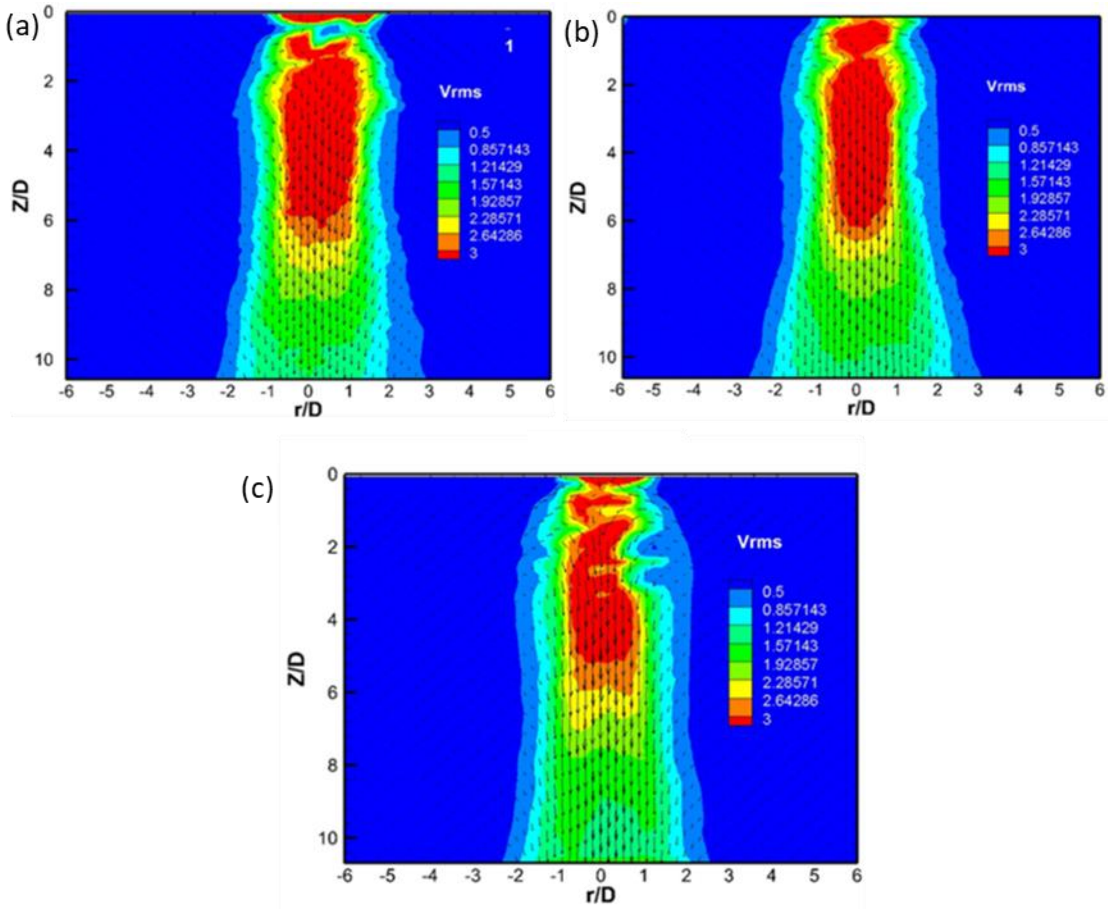

Figure 4.4: Ontour plots of mean velocity vector superimposed with V_{rms}(normal stress)for (a) multi-circular, (b) multi-oval and (c) circular-oval orifices.

4.4 Distribution of a Reynold stress for SJ:

4.4.1 Single orifice

This segment elucidates the mean velocity vector field for singular orifice and multi-orifice jets. The velocity vector field is superimposed with the Reynold stress contour. Reynolds stresses in an SJ orifice serve as indicators of the momentum exchange occurring between various fluid layers. These stresses arise from the turbulent fluctuations in streamwise and wall-normal velocity components, as detailed by Bhapkar *et al.* [40]. They signify the fluctuating components of the fluid velocity that contribute to turbulent flow. In the context of an SJ, Reynolds stresses provide insights into the intensity and nature of the turbulent fluctuations generated by the oscillating motion of the diaphragm and fluid expulsion through the orifice. Figure 4.5 clearly illustrates that in the proximity of the orifice, specifically at (Z/D<3), the Reynolds stress intensity is more pronounced for the oval orifice than the circular orifice. Conversely, in regions farther away from the orifice, i.e., (Z/D>7), the intensity of the circular orifice surpasses that of the oval orifice. This disparity indicates significant turbulence fluctuations and momentum exchange at (Z/D<2), favoring the oval orifice, while at (Z/D>7), the circular orifice exhibits higher turbulence. These observations align well with the details in the normal stress diagram presented in Figure 4.3, showing that the turbulence intensity for the oval orifice starts diminishing more than circular from (Z/D>7).

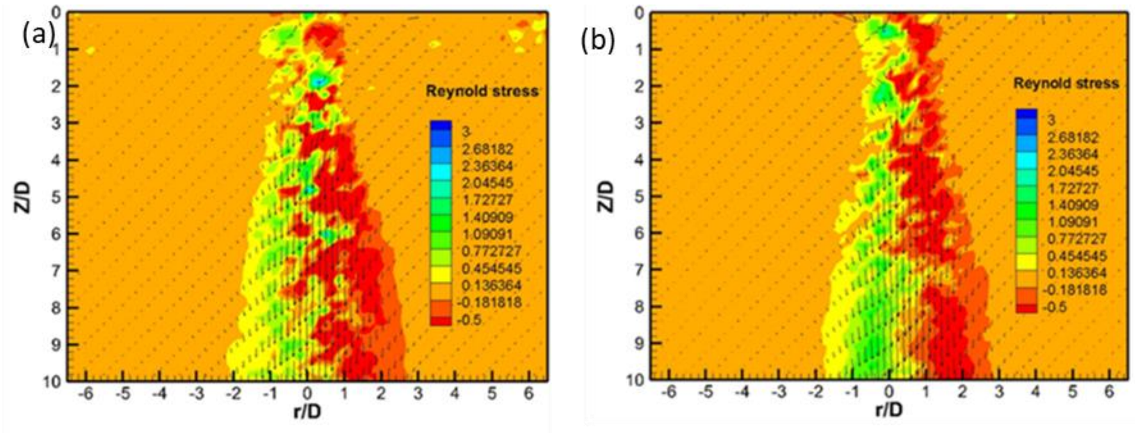

Figure 4.5: Contour for (a) circular and (b) oval orifices when mean velocity vector superimposed with Reynold stress.

4.4.2 Multi-orifice and mixed-orifice

Figure 4.6, depicting the mean velocity vector field overlaid with Reynolds stress contours for a multi-circular, multi-oval, and mixed-orifice jet, reveals interesting insights. Notably, when observing Figure 4.6, it becomes apparent that near the orifice (Z/D<3), the multi-orifice and mixed orifice configurations exhibit broader Reynolds stress contours compared to their single-orifice counterparts. This trend aligns with the observations made in Figure 4.4 regarding normal stress contours. The wider contours suggest that the multi-orifice and mixed-orifice configurations, owing to their inherent shapes, display heightened momentum exchange and turbulence compared to single-orifice configurations.

Interestingly, as we examine the Figure 4.4 along the axis at later regions, specifically at (Z/D>6), a notable observation is the drastic reduction in normal stress contours. Despite this reduction, the Reynolds stress contours indicate significant momentum exchange and turbulence. The reason is that the Reynolds shear stress is particularly sensitive to variations in vorticity because it reflects the momentum exchange between different layers of fluids. Vorticity plays a crucial role in generating these momentum fluctuations. As vorticity intensifies or changes its characteristics, it can significantly impact the Reynolds shear stresses in the SJ orifice. Figure 4.2 depicts multi-orifice configurations consistently exhibiting higher vortical structures throughout the flow. These structures generate the observed Reynolds stresses, showcasing the intricate relationship between vorticity, momentum exchange, and turbulence in the SJ orifice.

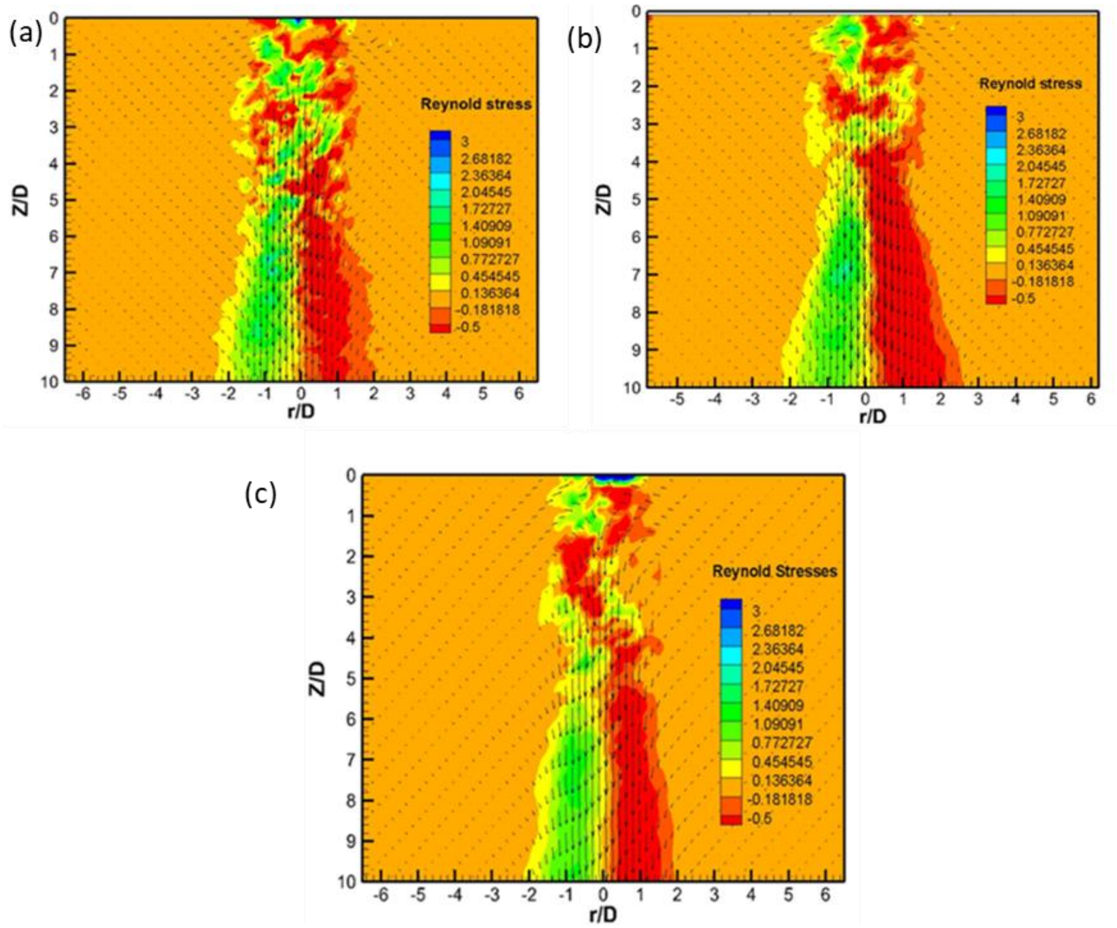

Figure 4.6: Mean velocity vector superimposed with Reynold stress contour for (a) multi-circular, (b) multi-oval and (c) circular-oval orifices.

4.5 Mass flow rate:

The mass entrainment properties of 5 different configurations, i.e., circular-oval (mixed orifice configuration with a circular orifice at the center as depicted in Figure 3.2), circular, and oval, are single geometric shapes at the center as orifices are determined by examining how the mass flow rate changes along the axial direction, as illustrated in Figure 4.7. The equivalent diameter of all orifice configurations is 10 mm. A single oval orifice at near jet regions exhibits higher entrainment than a single circular for the reasons mentioned in sections 4.2.1 and 4.2.2, such as axis-switching phenomena, pressure distributions around the orifice, etc. Figure 4.7 shows that compared to single-orifice jets, the multi-orifice configuration jet exhibits a greater entrainment rate in the nearby region, i.e., till Z/D<5.

The reason for the different behaviors lies in how the orifices are arranged. This results in more fluid flowing, explaining why the behavior changes with more orifices. Up to a distance represented by Z/D=12, the configuration multi-oval demonstrates a superior mass flow rate compared to the other configurations.

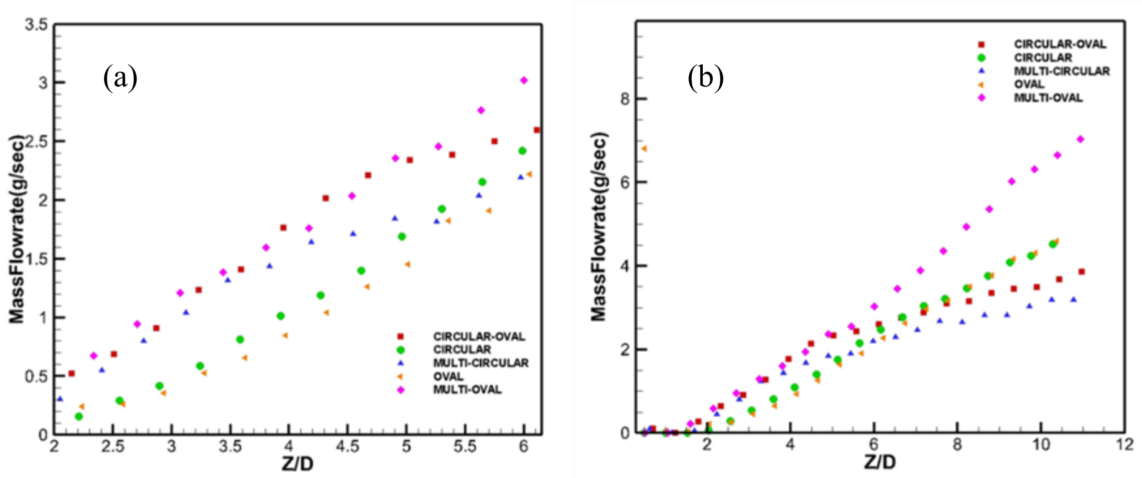

Figure 4.7: Mass flow rate of orifices along the axis of the SJ. (a) Till Z/D =6
(b) Till Z/D = 12

4.6 Jet centerline velocity

The analysis of the jet behavior from the orifice exit can be effectively conducted by examining the variation of centerline velocity (V_{cl}), as depicted in Figure 4.8. This plot serves as a valuable tool for understanding the dynamics of the jet flow. Close to the orifice, an intriguing observation emerges: the velocities exhibit a negative trend, indicating a flow directed back towards the orifice. This phenomenon indicates entrainment, suggesting that surrounding air or fluid is drawn into the jet stream near its origin point. Multi-orifices show higher centerline velocities than single-orifice configurations because multiple orifices allow for a higher total mass flow rate of fluid to be expelled and entrained into the SJ. This increased mass flow rate contributes to higher momentum and, consequently, higher centerline velocities. The centerline velocity is maximum for multi-oval orifice configurations and lower for single circular and single oval orifice configurations. At a distance of Z/D=2.5, the circular-oval orifice yields a higher V_{cl}. Beyond Z/D>2.5 Z/D<10, the multi-oval orifice configuration demonstrates superior V_{cl} performance. Subsequently, past Z/D>10, the oval orifice exhibits a rising trend in achieving higher V_{cl} values.

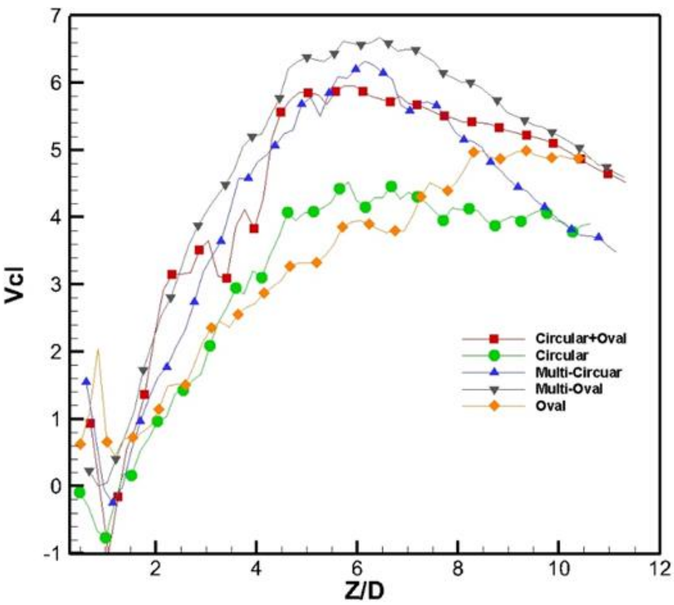

Figure 4.8: The jet centerline velocities (Vcl) versus Z/D of various orifices along the SJ axis.

4.7 Jet half width:

The jet half-width in the context of an SJ refers to the radial distance from the jet centerline to the point where the velocity of the SJ is half of its maximum centerline velocity, shown in Figure 3.4. The jet half-width is an important parameter that characterizes the lateral spreading of the SJ flow. It is important to note that the jet width, which refers to the lateral spread of the SJ, is inversely proportional to the centerline velocity. This means the jet width tends to decrease as the centerline velocity increases. The higher momentum generated by multiple orifices increases the centerline velocity and concentrates the fluid flow, leading to a narrower jet. From Figure 4.9, the half jet width of a multi-oval and multi-circular orifice surpasses that of a single circular orifice at lower orifice-to-plate distances due to the inherent design of the multi-oval shape, which initially provides a larger width. However, the jet width decreases as the centerline velocities of multi-orifices exceed those of singular orifices at later stages. This phenomenon occurs because the multi-oval orifice, with its unique shape, initially allows for a wider jet, but the higher velocities experienced later cause the width to reduce.

4.8 Heat transfer characteristics of SJ

This segment examines the heat transfer characteristics exhibited by single and multi-orifice configurations. The analysis entails the computation of dimensionless Nu to express heat transfer parameters quantitatively. The section explores the variation of the Nu_{avg}

concerning orifice-to-plate spacing and delves into the contour of Nu for different orifice-to-plate spacings. Experimental setups involve a single circular orifice plate with a 10 mm diameter and multiple orifice plates featuring 8 satellite configurations, each having a 3 mm center diameter and a 6.8 mm satellite diameter. To ensure a meaningful comparison, the hydraulic diameter of the multi-orifice plate remains consistent with the single-orifice diameter. The center and satellite diameters are positioned equidistantly at a 12 mm pitch circle radius. The experimental conditions remain standardized when operating at an 80 Hz excitation frequency and a 4 V amplitude.

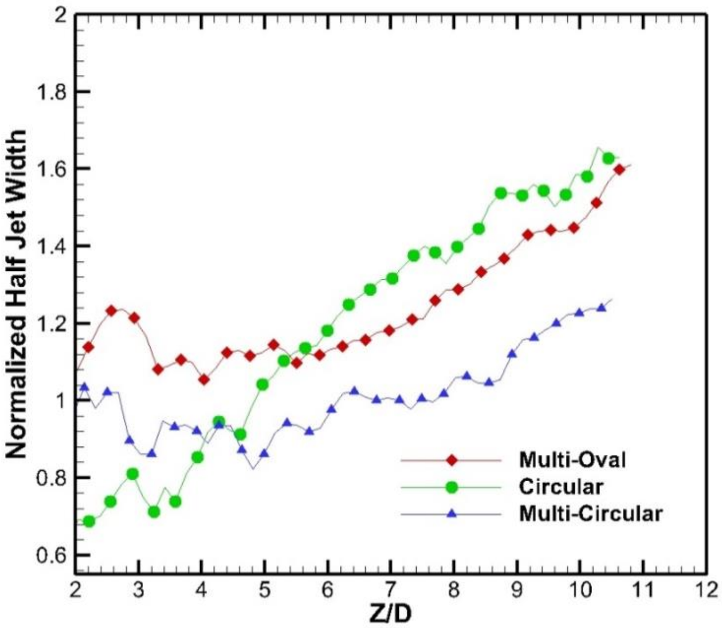

Figure 4.9: Jet half width of orifices along the axis of the SJ.

4.9 Heat transfer characteristics of single orifice SJ

In this section, we explore the changes in the Nu_{avg} concerning the orifice-to-plate spacing. Figure 4.10 visually depicts how Nu_{avg} fluctuates with variations in the orifice-to-plate spacing, specifically for a single circular orifice jet. The graphical representation in Figure 4.10 underscores a noteworthy observation: up to a dimensionless parameter Z/D value of 6, the oval orifice exhibits superior performance compared to its circular counterpart. This trend is corroborated by the flow characteristic contours, including vorticity, root-mean-square velocity (V_{rms}), and Reynolds stresses. The underlying rationale behind this enhanced heat transfer lies in the manifestation of axis-switching phenomena and flow separation occurring at the edges of the oval orifice. These phenomena collectively contribute to more favorable heat transfer rates, providing valuable insights into the intricate dynamics influencing the thermal performance of these orifice configurations. In the case of a single oval orifice, the peak value of the Nu_{avg} is noted at Z/D=7. Conversely, the maximum Nu_{avg} is attained at Z/D=11 for a circular orifice. This discrepancy in the optimal orifice-to-plate spacing highlights distinct heat transfer characteristics for each geometry, indicating the influence of shape-specific fluid dynamics and thermal behaviors on the overall performance of the orifice configurations.

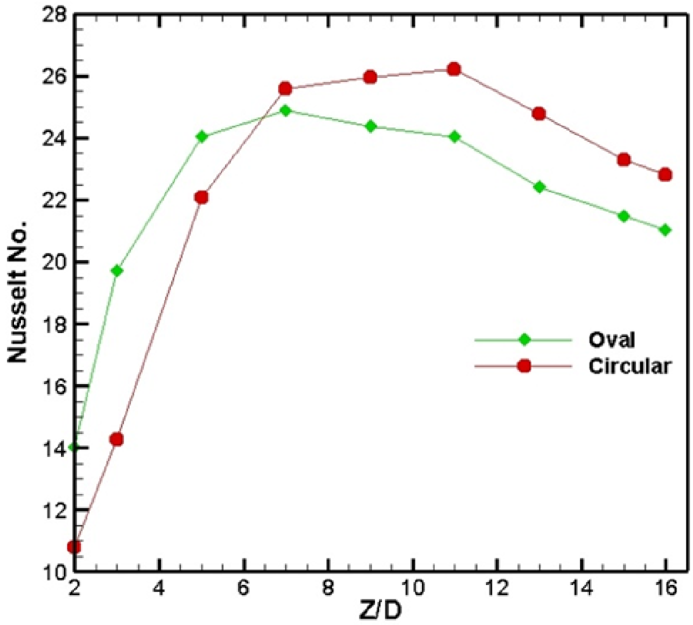

Figure 4.10: Nu_{avg} as a function of Z/D (orifice-to-plate spacing) for single-orifice configurations

4.10 Heat Transfer Characteristics of Multi-orifice SJ:

This work investigation unequivocally validates multi-orifice configurations' enhanced heat transfer attributes, particularly evident at Lower orifice-to-surface spacings. The trends are graphically represented in Figure 4.11, reinforcing the efficacy of multi-circular orifices compared to their single counterparts. Up to Z/D=5, the multi-circular orifice consistently outperforms the single circular orifice, showcasing higher Nu_{avg}. A pivotal highlight emerges at Z/D=2, where the multi-circular orifice demonstrates a remarkable 29 percent increase in heat transfer rate compared to the single circular configuration. Numerical values substantiate this noteworthy improvement and are visually apparent in the flow characteristics. They are further elucidating the intricate dynamics contributing to the heightened heat transfer efficiency of the multi-orifice setup. In summary, the combined effects of greater shear, intensified turbulence, and enhanced entrainment from satellite orifices collectively contribute to the superior heat transfer characteristics observed in multi-circular orifice configurations, especially at lower orifice-to-surface spacings.

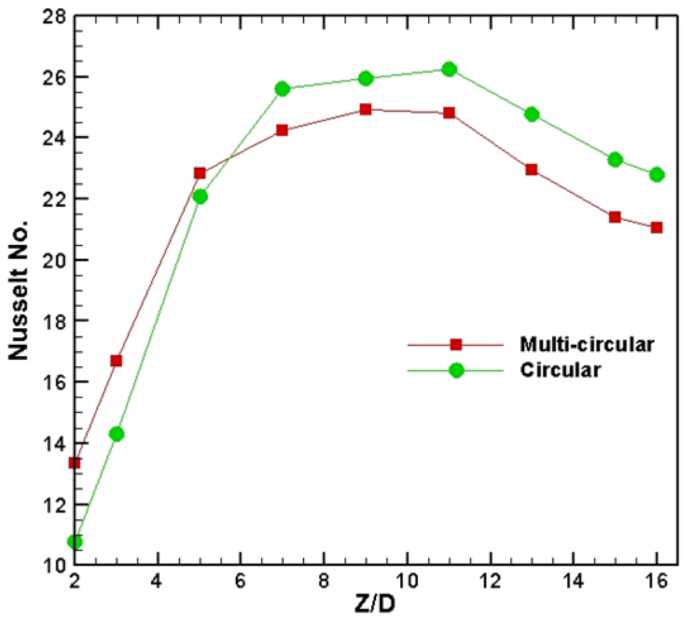

Figure 4.11: Nu_{avg} versus Z/D (orifice-to-plate spacing) for single-circular and multi-circular configurations

Figure 4.12(a) comprehensively compares heat transfer characteristics between multi-circular and multi-oval configurations. Notably, until Z/D=16, the multi-oval configuration consistently demonstrates superior heat transfer characteristics compared to its multi-circular counterpart. This distinction is discernible in the flow characteristics, including Reynolds stresses, Vrms-contour, and vorticity contours, with their contours depicted up to Z/D=10. At lower surface spacings, specifically at Z/D=2, the multi-oval orifice exhibits a remarkable 22 percent higher heat transfer rate than the multi-circular configuration. This early-stage advantage indicates the enhanced convective heat transfer efficiency facilitated by the distinctive geometry of the multi-oval orifice. Moreover, the analysis of the Nu_{avg} highlights the optimal performance of the multi-oval orifice at Z/D=7, showcasing the highest heat transfer rates within the observed range. In contrast, the multi-circular configuration reaches its peak heat transfer rate slightly later, at Z/D=11. These results highlight how the shape of the orifice and how heat moves around it are closely connected. This information is vital for making multi-orifice setups work better when we need heat to be transferred efficiently. It gives us valuable ideas for designing and improving these setups in real-world applications where good thermal performance is crucial.

4.11 Heat Transfer Characteristics of Mixed-orifice SJ

Figure 4.12(b) A noteworthy observation emerges: at Z/D=2, the multi-oval configuration outperforms all other orifice types, while the circular orifice exhibits comparatively lower heat transfer characteristics. The mixed orifice configuration (combining circular and oval shapes) demonstrates an interesting trend. It closely mirrors the heat transfer characteristics of the oval orifice at lower Z/D values, up to Z/D=7, and transitions to resemble the circular orifice at higher Z/D values. This dynamic behavior suggests that the circular-oval or mixed orifice configuration adapts its heat transfer performance based on the specific orifice-to-plate spacing. At lower spacings, it tends to emulate the superior characteristics of the oval orifice, while at higher spacings, it converges towards the thermal behavior exhibited by the circular orifice.

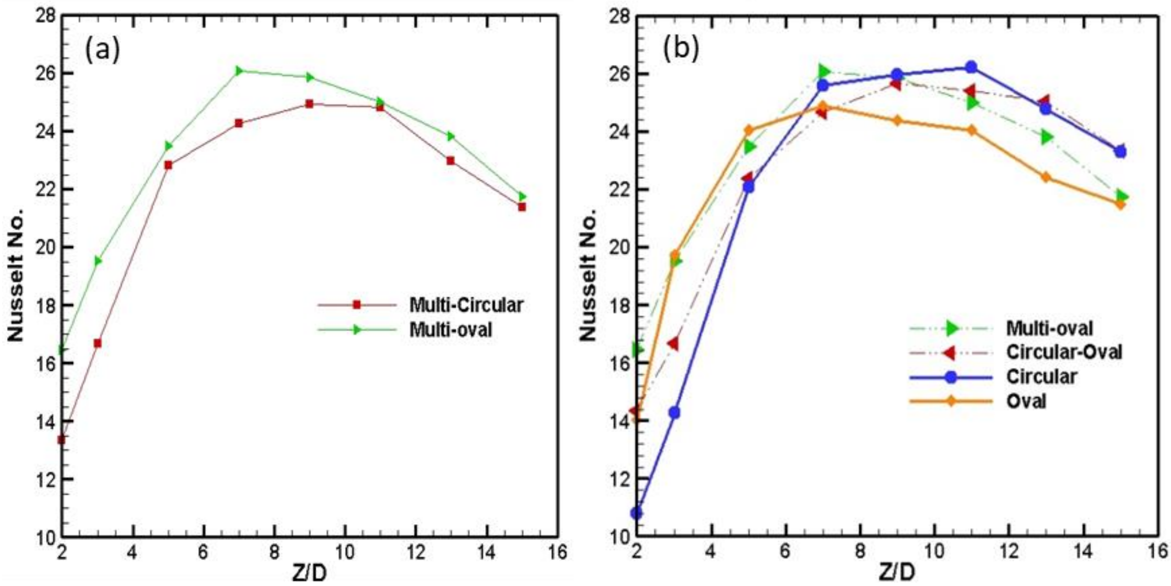

Figure 4.12: (a) Plots for Nu_{avg} with Z/D (orifice-to-plate spacing) for multi-circular and multi-oval configurations. (b) comparison of best orifices Nu_{avg} as a function of Z/D (orifice-to-plate spacing) plots for single, multi and mixed-orifice configurations.

Chapter 5

Conclusions and the scope for future work

In this experimental study employing PIV, the distinct flow characteristics associated with various orifice configurations are studied. The heat transfer characteristics are explained using the flow behavior of these different configurations. The study serves as a foundation for understanding the potential impact of these configurations on heat transfer characteristics. The investigation draws comparisons between the outcomes of multi-orifice and mixed-orifice configurations with those of single-orifice configurations. The following key conclusions are drawn from the results of the study

- In the comparison of different orifice configurations, specifically the multi-oval and mixed orifice designs, we observed increased vortices compared to single orifice setups, particularly at the orifice exit within the range of Z/D=0-2. Among all configurations, the Mixed-orifice shape demonstrated the presence of vortices to a greater extent i.e. $Z/D > 8$ along the axial direction.
- Building on the previous literature, our study affirms that multi-orifice configurations exhibit superior heat transfer characteristics, especially at lower orifice-to-surface spacings. This can be attributed, in part, to the normal stress (Vrms) distribution in the flow field. Both the multi-orifice and mixed-orifice configurations feature thicker and wider Vrms distribution compared to single-orifice configurations. These contours indicate the presence of greater turbulence, particularly evident until $Z/D <6$.
- The multi-oval orifice showcases superior momentum exchange between fluid layers, surpassing the performance of all other orifice configurations. In proximity to the orifice exit, both multi and mixed-orifice shapes show higher mass entrainment.
- The centerline velocity variation demonstrates that multi-orifice configurations consistently exhibit higher centerline velocities in comparison to single-orifice configurations. This can be attributed to the higher total mass flow rate entrained by the multi-orifice setups.
- After $Z/D > 6$, the single circular orifice demonstrates a broader jet width, influenced by its lower centerline velocities. In proximity to the orifice exit, multi-circular and multi-oval orifices exhibit greater jet width due to their inherent shapes.

- The multi-circular orifice shows ~29 % increase in heat transfer rate observed at Z/D = 2. It shows the effectiveness of multi-orifice configurations, attributed to intensified turbulence and enhanced entrainment from satellite orifices.
- The multi-oval orifice configuration demonstrates superior heat transfer performance compared to other types, especially at Z/D = 2, while the mixed-orifice configuration exhibits a transition in heat transfer characteristics, resembling oval or circular orifices depending on the orifice-to-plate spacing.

5.2 Scope of future work

The scope of future work in SJs encompasses diverse and promising applications, ranging from turbine cooling and electric vehicle thermal management to innovative aerosol-based cooling solutions. By advancing research in these areas, we can contribute to developing more efficient, sustainable, and reliable cooling technologies with widespread industrial and commercial implications.

- **Integration of SJs with mist for turbine cooling or turbomachinery**

One promising area of future work involves integrating SJs with mist for turbine cooling or turbomachinery applications. Combining SJs with a misting system can enhance the cooling efficiency and effectiveness of turbine components subjected to high temperatures by forming a protective mist-coated layer that prevents the blade from being in direct contact with hot fluid. The misting of fine water droplets can complement the airflow generated by SJs, improving heat transfer and thermal management in critical turbine components. This integrated approach can optimize the performance and durability of turbines in various industrial sectors, including power generation and aerospace.

- **Electric vehicle cooling using SJs**

With the rise of electric vehicles poised to dominate the conventional internal combustion engine market, there is a pressing need for efficient cooling solutions for electric motors. SJs offer a promising method for actively cooling electric vehicle components, including motors and battery systems. By deploying SJs strategically within EVs, we can enhance thermal management, mitigate heat-related issues, and optimize electric propulsion systems' overall efficiency and lifespan. This future work aligns with the growing demand for sustainable and high-performance cooling technologies in the automotive industry.

- **Employment of SJs with aerosol for cooling applications**

Another innovative direction for future research involves utilizing SJs with aerosol particles for advanced cooling applications. Aerosol-based cooling systems leverage the dispersal of fine particles in SJ-generated airflow to enhance heat transfer rates and cooling efficiency. This approach offers potential advantages in terms of scalability, adaptability, and energy efficiency compared to traditional cooling methods. Exploring SJs combined with aerosol technologies opens up new possibilities for cooling sensitive electronics, heat exchangers, and other thermal management systems across various industries.

References

[1] A. Pal, Y.K. Joshi, M.H. Beitelmal, C.D. Patel and T.M. Wenger, Design and performance evaluation of a compact thermosyphon, IEEE Trans. Components Package. Technol. 25 (2002), pp. 601–607.

[2] X. Wei, IMECE2004-62509, (2016), pp. 1–7.

[3] S. V. Garimella, V. Singhal and D. Liu, On-chip thermal management with microchannel heat sinks and integrated micropumps, Proc. IEEE 94(2006), pp. 1534–1548.

[4] R.E. Simons and R.C. Chu, Application of thermoelectric cooling to electronic equipment: A review and analysis, Annu. IEEE Semicond. Therm. Meas. Manag. Symp. (2000), pp. 1–9.

[5] M. Chaudhari, B. Puranik, and A. Agrawal, "Heat transfer characteristics of synthetic jet impingement cooling," Int J Heat Mass Transfer, vol. 53, no. 5–6, pp. 1057–1069, Feb. 2010, doi: 10.1016/j.ijheatmasstransfer.2009.11.005.

[6] C. M. Crispo, C. S. Greco, and G. Cardone, "Convective heat transfer in circular and chevron impinging synthetic jets," Int. J. Heat Mass Transfer 126, 969–979 (2018)

[7] R. Mahalingam and A. Glezer, "Design and thermal characteristics of a synthetic jet ejector heat sink," J. Electron. Package. 127(2), 172 (2005).

[8] G. Paolillo, C. S. Greco, and G. Cardone, "Impingement heat transfer of quadruple synthetic jets," Int. J. Heat Mass Transfer 135, 1192–1206 (2019).

[9] A. Pavlova and M. Amitay, "Electronic cooling using synthetic jet impingement," J. Heat Transfer 128(9), 897 (2006).

[10] Pack, L. G., and Seifert, A., "Periodic Excitation for Jet Vectoring and Enhanced Spreading," Journal of Aircraft, Vol. 38, No. 3, 2001, pp. 486–495.

[11] Cater, J. E., & Soria, J., "The Evolution of Round Zero-Net-Mass-Flux Jets," Journal of Fluid Mechanics, Vol. 472, 2002, pp. 167–200.

[12] Strzelczyk, P; Gil, P (2016). Properties of velocity field in the vicinity of synthetic jet generator. Journal of Physics: Conference Series, 760(), 012029–. doi:10.1088/1742-6596/760/1/012029

[13] M. Chaudhari, B. Puranik, and A. Agrawal, "Heat transfer characteristics of synthetic jet impingement cooling," Int J Heat Mass Transfer, vol. 53, no. 5–6, pp. 1057–1069, Feb. 2010, doi: 10.1016/j.ijheatmasstransfer.2009.11.005.

[14] Mane, P., Mossi, K., Rostami, A., Bryant, R. and Castro, N., 2007. Piezoelectric actuators as synthetic jets: Cavity dimension effects. Journal of Intelligent Material Systems and Structures, 18(11), pp.1175-1190.
[15] Paolillo, G., Greco, C.S. and Cardone, G., 2017. Novel quadruple synthetic jet device: Flow field and acoustic behavior. AIAA Journal, 55(7), pp.2241-2253.
[16] Arshad, Adeel; Jabbal, Mark; Yan, Yuying (2020). Synthetic jet actuators for heat transfer enhancement – A critical review. International Journal of Heat and Mass Transfer, *146(), 118815–*. doi:10.1016/j.ijheatmasstransfer.2019.118815
[17] T. Murugan, M. Deyashi, S. Dey, S.C. Rana, P. Chatterjee, Recent developments on synthetic jets, Defence Sci. J. 66 (5) (2016) 489, https://doi.org/10.14429/ dsj.66.9776.
[18] A. Pavlova and M. Amitay, "Electronic cooling using synthetic jet impingement," J. Heat Transfer, vol. 128, no. 9, pp. 897–907, 2006, doi: 10.1115/1.2241889.
[19] J. Stephen Campbell, J. Boeing North American, W. Z. Black, A. Glezer, and J. G. Hartley, "Thermal Management of a Laptop Computer with Synthetic Air Microjets."
[20] H. Martin, "Heat and Mass Transfer between Impinging Gas Jets and Solid Surfaces", Advances in Heat Transfer,1977.
[21] K. Jambunathan, et al, "A Review of Heat Transfer Data for Single Circular Jet Impingement", Inti. J. of Heat and
Fluid Flow, 13(2), 106-115, June, 1992.
[22] **T.** Hamadah, "Impingement Cooling of a Simulated Electronics Package with a Square Array of Round Jets", Heat Transfer in Electronics, ASME **HTD** Vol. **1** 1 **1,** 107-112,1989.
[23] R. Nevins and H. Ball, "Heat Transfer between a Flat Plate and a Pulsating Impinging Jet, The 1961 National Heat Transfer Conference, *60,5* 10-516, 1961.
[24] A. Glezer, Some aspects of aerodynamic flow control using synthetic-jet actuation, Philos. Trans. Roy. Soc. Lond. A: Math. Phys. Eng. Sci. 369 (2011) 1476–1494
[25] N. Ramos-Pedroza, W. MacKunis and M. Reyhanoglu, Synthetic Jet Actuator-Based Aircraft Tracking Using a Continuous Robust Nonlinear Control Strategy, Int. J. Aerosp. Eng. 2017 (2017).
[26] G. Zhao, Q. Zhao, Y. Gu and X. Chen, Experimental investigations for parametric effects of dual synthetic jets on delaying stall of a thick airfoil, Chinese J. Aeronaut. 29 (2016), pp. 346–357.
[27] TT Rice, K. Taylor and M. Amitay, Pulse modulation of synthetic jet actuators for separation control, Phys. Rev. Fluids 6 (2021), pp. 1–28.

[28] J.R. Guarino and V.P. Manno, Characterization of laminar jet impingement cooling in portable computer applications, Annu. IEEE Semicond. Therm. Meas. Manag. Symp. 25 (2001), pp. 337–346.
[29] T. Mahmud, J.N. Haque, K.J. Roberts, D. Rhodes and D. Wilkinson, Measurements and modelling of free-surface turbulent flows induced by a magnetic stirrer in an unbaffled stirred tank reactor, Chem. Eng. Sci. 64 (2009), pp. 4197–4209.
[30] L. Le Van, C. Nguyen Nhu, T.N. Tai, T. Xuan DInh, C.D. Tran, L.D. Bao et al., Liquid Pumping and Mixing by Pzt Synthetic Jet, 2019 20th Int. Conf. Solid-State Sensors, Actuators Microsystems Eurosensors XXXIII, TRANSDUCERS 2019 EUROSENSORS XXXIII (2019), pp. 198–201.
[31] M. Al-Atabi, Experimental investigation of the use of synthetic jets for mixing in vessels, J. Fluids Eng. Trans. ASME 133 (2011), pp. 2011–2014.
[32] T. M. Dauphinee, "Acoustic air pump," Review of Scientific Instruments, vol. 28, no. 6, p. 452, 1957, doi: 10.1063/1.1715904.
[33] P. Sharma, P. K. Singh, S. K. Sahu, and H. Yadav, "A Critical Review on Flow and Heat Transfer Characteristics of Synthetic Jet," Transactions of the Indian National Academy of Engineering, vol. 7, no. 1, pp. 61–92, 2022, doi: 10.1007/s41403-021-00264-5.
[34] G. Krishan, K. C. Aw, and R. N. Sharma, "Synthetic jet impingement heat transfer enhancement – A review," Applied Thermal Engineering, vol. 149. Elsevier Ltd, pp. 1305–1323, Feb. 25, 2019. doi: 10.1016/j.applthermaleng.2018.12.134.
[35] Hong, M. H., Cheng, S. Y., & Zhong, S. (2020). Effect of geometric parameters on synthetic jet: A review. Physics of Fluids, 32(3).
[36] Gutmark, E. J., and Grinstein, F. F., "Flow control with noncircular jets," Annu. Rev. Fluid Mech. 31(1), 239–272 (1999).
[37] Wang, L., Feng, L. H., Wang, J. J., and Li, T., "Characteristics and mechanism of mixing enhancement for noncircular synthetic jets at low Reynolds number," Exp. Therm. Fluid Sci. 98, 731–743 (2018).
[38] Michalke, A., "Instability of a compressible circular free jet with consideration of the influence of the jet boundary layer thickness," Report No. NASA-TM-75190, 1977
[39] Chaudhari, M., Puranik, B., & Agrawal, A. (2010). Heat transfer characteristics of synthetic jet impingement cooling. *International Journal of Heat and Mass Transfer*, *53*(5-6), 1057-1069.

[40] Bhapkar, U. S., Mishra, A., Yadav, H., & Agrawal, A. (2022). Effect of orifice shape on impinging synthetic jet. *Physics of Fluids*, *34*(8).
[41] Bhapkar, U. S., Srivastava, A., and Agrawal, A., "Acoustic and heat transfer characteristics of an impinging elliptical synthetic jet generated by acoustic actuator," Int. J. Heat Mass Transfer 79, 12–23 (2014b).
[42] Chaudhari, M., Puranik, B., & Agrawal, A. (2011). Multiple orifice synthetic jet for improvement in impingement heat transfer. *International Journal of Heat and Mass Transfer*, *54*(9-10), 2056-2065.
[43] Lee, J., and Lee, S., "The effect of nozzle aspect ratio on stagnation region heat transfer characteristics of elliptic impinging jet," Int. J. Heat Mass Transfer 43, 555–575 (2000).
[44] Zaman, K., "Spreading characteristics of compressible jets from nozzles of various geometries," J. Fluid Mech. 383, 197–228 (1999).
[45] LD. Mangate and M.B. Chaudhari, Heat transfer and acoustic study of impinging synthetic jet using diamond and oval shape orifice, Int. J. Therm. Sci. 89 (2015), pp. 100–109.
[46] J. Vejrazka, J. Tihon, P. Mart, and V. Sobolík, "Effect of an external excitation on the flow structure in a circular impinging jet," Phys. Fluids, vol. 17, no. 10, 2005, doi: 10.1063/1.2084207
[47] Pawan Sharma, Dnyanesh Mirikar, Jitendra K. Choudhary, Raghuvamsi Bokka, Jay Joshi, Santosh K. Sahu and Harekrishna Yadav, "Numerical studies on the influence of Strouhal number on the flow characteristics of Synthetic Jet impingement".
[48] H. Yadav, A. Joshi, M. Chaudhari, and A. Agrawal, "An experimental study of a multi-orifice synthetic jet with application to cooling of compact devices," *AIP Adv*, vol. 9, no. 12, Dec. 2019, Doi: 10.1063/1.5128776.
[49] Rylatt, D I; O'Donovan, T S (2014). The effects of stroke length and Reynolds number on heat transfer to a ducted confined and semi-confined synthetic air jet. Journal of Physics: Conference Series, 525(), 012012–. doi:10.1088/1742-6596/525/1/012012
[50] C. Y. Lee and D. B. Goldstein, "Two-dimensional synthetic jet simulation," AIAA J. 40(3), 510 (2002).
[51] Raffel, M., Willert, C. E., Scarano, F., Kähler, C. J., Wereley, S. T., & Kompenhans,(2018). Particle image velocimetry: a practical guide. Springer.)
[52] U. S. Bhapkar, A. Srivastava, and A. Agrawal, "Proper cavity shape can mitigate confinement effect in synthetic jet impingement cooling," Exp. Therm. Fluid Sci. 68, 392–401 (2015)

[53] Mallinson, S. G., Reizes, J. A., Hong, G., & Westbury, P. S. (2004). Analysis of hot-wire anemometry data obtained in a synthetic jet flow. Experimental thermal and fluid science, 28(4), 265-272.
[54] L. Mangate, H. Yadav, A. Agrawal, and M. Chaudhari, "Experimental investigation on thermal and flow characteristics of synthetic jet with multiple-orifice of different shapes," Int. J. Therm. Sci. 140, 344–357 (2019).
[55] Adrian, R.J., Westerweel, J., 2011. Particle Image Velocimetry. Cambridge University Press, Cambridge.
[56] C. M. Sewatkar, R. Patel, A. Sharma, and A. Agrawal, "Flow around six in-line square cylinders," J. Fluid Mech. 710, 195–233 (2012).
[57] H. W. Coleman, W. Glenn. Steele, and H. W. Coleman, Experimentation, validation, and uncertainty analysis for engineers. John Wiley & Sons, 2009.
[58] M. Raffel, U. Seelhorstt, and C. Willert, "Vortical flow structures at a helicopter rotor model measured by LDV and PIV," 1998.
[59] L. Wang, J. Hejcik, and B. Sunden, "PIV measurement of separated flow in a square channel with streamwise periodic ribs on one wall," J. Fluids Eng. 129, 834–841 (2007).
[60] P. K. Singh, S. K. Sahu, P. K. Upadhyay, and S. Singh, "Experimental and numerical investigation of the thermal performance of impinging synthetic jets with different waveforms," *Experimental Heat Transfer*, vol. 36, no. 2, pp. 121–142, 2023, doi: 10.1080/08916152.2021.1984341.
[61] P. Sharma, S. K. Sahu, and H. Yadav, "The flow and heat transfer behavior of synthetic jets with star shaped orifice of different lobes," *International Journal of Thermal Sciences*, vol. 193, Nov. 2023, doi: 10.1016/j.ijthermalsci.2023.108523.
[62] P. Sharma, S. K. Sahu, and H. Yadav, "Experimental investigation of flow and thermal characteristics of synthetic jet issuing from sharp-edged orifices," *Experimental Heat Transfer,* 2022, doi: 10.1080/08916152.2022.2105449.
[63] Ho, C. M., & Gutmark, E. (1987). Vortex induction and mass entrainment in a small-aspect-ratio elliptic jet. Journal of Fluid mechanics, 179, 383-405.